Anionic Phospholipids Modulate Hepatitis C Virus Core Protein Assembly on Lipid Membranes

Titas Mandal[1], Bastian Albrecht[2] and Salvatore Chiantia[1,§]

[1]University of Potsdam, Institute of Biochemistry and Biology, Karl-Liebknecht-Straße 24-25, 14476 Potsdam, Germany

[2] Institute of Chemistry, Technical University of Berlin, Straße des 17. Juni 135, 10623 Berlin, Germany

§ Email: chiantia@uni-potsdam.de

Abstract

Hepatitis C virus (HCV) genome codes for various proteins essential to its replication cycle. Among these, the core protein (HCC) forms the capsid via organised multimerization, thereby guiding viral assembly. This process depends on the dynamic localisation of HCC between the endoplasmic reticulum bilayer membrane and the lipid droplet monolayer. While past studies have examined the role of some HCC structural properties and other viral and host proteins in the assembly process, the contribution of lipid molecules was not thoroughly investigated yet. Since specific lipids are upregulated during HCV infection, it is reasonable that these molecules might play an important role for virus fitness and infection progression. In this study, we have addressed this topic and, specifically, how HCC-lipid interactions might impact HCC-HCC interactions. Using *in vitro* models and quantitative fluorescence microscopy techniques, we investigated HCC binding affinity to lipid membranes, multimerization and lateral diffusivity. Our results reveal the specificity of HCC interactions with anionic phospholipids (PLs) in terms of binding to monolayers and bilayers. Furthermore, our analysis shows that anionic PLs enhance HCC multimerization and, therefore, might drive lateral assembly for capsid formation. These results not only provide insights into the lipid-driven regulation of HCV assembly and identify anionic PLs as potential modulators of the viral replications cycle, but also highlight a previously unrecognised role of PL composition in HCC-membrane interaction.

Introduction

Infection by Hepatitis C virus (HCV) is associated to severe liver disease and poses a serious global health challenge, due to the absence of vaccines and broadly accessible targeted medications [1–3]. HCV is an enveloped virus with a 9.6 kb positive-sense RNA that codes for various viral proteins, including the Core protein (HCC) [4]. HCC forms the structural subunits of the viral capsid, i.e. an icosahedral protective shell between the viral genome and the lipid envelope of the virus [5]. Additionally, HCC plays fundamental roles in viral assembly [4–7], as well as hijacking of several host cellular pathways for sustaining the viral replication cycle [8–13].

HCV RNA translates into a polyprotein which produces ten individual viral proteins upon cleavage at specific sites by the host and viral peptidases [11]. In this regard, HCC is derived from the N-terminus of this polyprotein via the action of a host peptidase [11,14,15]. The 191 amino acids (aa) long nascent HCC is targeted to the endoplasmic reticulum (ER) membrane owing to the presence of the C-terminal signal peptide (SP) domain 20, which also acts as a bilayer transmembrane anchor [4,16]. Besides the SP, HCC includes two more domains: D1 and D2 [17]. D1 is a larger (117 aa) hydrophilic domain enriched in basic amino acids. D2 is a shorter (54 aa) and more hydrophobic domain that consists of two amphipathic helices (H1 and H2) connected by a hydrophilic loop (HL) [16–18]. Owing to the presence of the basic residues, D1exhibits diverse interactions with the viral RNA [19–21] and, subsequently, promotes the formation of nucleocapsid [4,22]. Additionally, several regions of D1 promote homotypic ionic interactions that form homo-multimers, necessary for capsid formation [6]. The D2 domain, on the other hand, interacts with lipid membranes through its amphipathic character [16,23]. D2 additionally promotes HCC homo-dimer formation through a disulphide bond between the Cysteine residues (Cys128) of each protein [18]. Such dimers play a notable role in the viral assembly by establishing the foundation for a stable nucleocapsid [5,18,24]. As a part of the HCV replication cycle, HCC exhibits an organized dynamic partition between the ER bilayer membrane and lipid droplet (LD) monolayers [14–16,25,26]. At the ER membrane, SP-peptidase-mediated cleavage of SP gives rise to the mature form of the HCC (171 aa) [16], which is subsequently escorted to the LD surface by host proteins [25,27]. The HCC-LD relationship is of paramount importance for the viral assembly process [15]. For instance, HCC starts assembling into highly ordered multimers while on the surface of LDs, marking the first step of the viral assembly [15]. Interestingly, arresting this step disrupts the viral life cycle [15] by inhibiting the transfer of HCC from the LD back to the ER [28–30]. HCC multimer re-targeting to the ER membrane is actively mediated by other HCV proteins [4,14,26], and this translocation has been shown to assist in the late steps of the viral life cycle [31]. These include synchronised packaging of the viral RNA with the core multimers and other viral proteins to form new viral particles [14,26], which subsequently transit into the host secretory pathway [4,22,30,32]. Interestingly, HCC itself can form virions, independent of other viral proteins [15], indicating the fundamental role of this protein in virion production.

While (protein) host factors involved in HCC trafficking between ER and LDs were studied extensively [14–16,25,26], the influence of lipids in determining HCC localization and viral assembly are not well understood. Recent findings highlighted the role of neutral lipids such as triglycerides (TGs) in promoting D2 binding to artificial LDs (ALDs) or membrane bilayer models (i.e., giant unilamellar vesicles (GUVs)) [33]. On the other hand, zwitterionic-phospholipids (PLs) such as phosphatidylcholine/ phosphatidylethanolamine were shown to hinder D2 interactions with both monolayers and bilayers [33]. Otherwise, no detailed information is available regarding how specific PLs might affect HCC-lipid and HCC-HCC interactions. In this context, it is worth mentioning that, as a part of its host cellular pathway hijacking process, HCV upregulates the synthesis of certain anionic PLs such as phosphoinositides (which are in fact identified as "clinical hallmark" of HCV infection) [34–36]. Despite their significant involvement in various stages of the HCV replication cycle [37], the possible contribution of anionic PLs in HCC trafficking and subsequent assembly is not known.

In this study, we clarify the role of anionic PLs in HCV assembly, using *in vitro* approaches. To this aim, we investigated the interaction of fluorescently labelled recombinant HCC [18] with model membranes, such as GUVs and ALDs representing PL bilayers (ER membrane) and monolayers, respectively [33,38,39]. Specifically, we quantified HCC interactions with ALDs and GUVs in terms of binding affinity, multimerization, lateral dynamics and assembly using fluorescence fluctuation microscopy methods, such as line-scan fluorescence correlation spectroscopy (lsFCS) [40,41] and image correlation spectroscopy (ICS) [42]. These methods were successfully used in the past to study viral protein assembly, *in vivo* localisation and dynamics [41,43,44]. By performing such a systematic analysis of the interactions between HCC and model membrane platforms composed of different PLs, we show that anionic PLs strongly influence HCC multimerization at the surface of LD as well as PL bilayers, and, therefore, might play a fundamental role in the assembly of HCV.

Material and Methods

1. Materials

For the preparation of ALDs and GUVs, the detergent n-dodecyl β-D-maltoside (DDM) and the following lipids were purchased from Avanti Polar Lipids (Alabaster, AL, USA): 1,2-dioleoyl-sn-glycero-3-phosphocholine (DOPC), sphingomyelin (Milk, Bovine), 1,2-dioleoyl-sn-glycero-3-phospho-L-serine (DOPS), L-α-phosphatidylinositol-4-phosphate (Brain PI(4)P), L-α-phosphatidylinositol-4,5-bisphosphate (Brain PI(4,5)P2), 1-oleoyl-2-(6-((4,4-difluoro-1,3-dimethyl-5-(4-methoxyphenyl)-4-bora-3a,4a-diaza-s-indacene-2-propionyl)amino)hexanoyl)-sn-glycero-3-phosphocholine (TF-PC) and 1,2-distearoyl-sn-glycero-3-phosphoethanolamine-N-lissamine rhodamine B sulfonyl-ammonium salt (Rh-PE). Glycerine trioleate (Triolein) for the preparation of LDs, Alexa Fluor® 488 dye (AF488) and Alexa Fluor® 555 dye

(AF555) for the calibration of excitation beam waist, and streptavidin for GUV chamber coating were purchased from ThermoFisher Scientific (Waltham, MA, USA). Sucrose for electroformation was purchased from PanReac Applichem GmbH (Darmstadt, Germany). Tris-HCL, magnesium chloride ($MgCl_2$), urea, β-mercaptoethanol, Bovine serum albumin (BSA) for GUV chamber coating, disodium phosphate and monosodium phosphate for sodium phosphate buffer (NaP) preparation, ethanol for monolayer glass chamber cleaning and β-mercaptoethanol were purchased from Carl Roth GmbH (Karlsruhe, Germany). EDTA-free protease inhibitor cocktail tablet was purchased from Roche Holding AG (Basel, Switzerland).

2. Vector expression and protein purification

The plasmid CMV-FLAG-Core-R (catalog no. 22480) for expressing HCC (genotype 1b), was purchased from Addgene (Watertown, MA, USA). A forward primer with Nde1 (TAACATATG**ATGAGCACGAATCCTAAACCTC**) and reverse primer with BamH1 (TTAGGATCC**CAGATTCCCTGTTGCATAGTTC**) cleavage site was designed to amplify a 507-bp nucleotide fragment corresponding to the 169 aa long HCC [18] from the purchased plasmid, using PCR. This amplified segment was then ligated into pET-15b vector (Novagene, catalog no. 70755, Burlington, MA, USA) and transformed into *E.coli* (BL21 AI strain) for protein expression. N-terminal 6X-Histidine tagged HCC was expressed and purified following the available protocol by Boulant *et al.* [18] with slight modifications.
E.coli BL21 AI transformants were incubated in LB medium mixed with 100 µg/mL ampicillin at 37 °C (120 rpm) until the growth culture optical density (at 600 nm) reached ~0.7. Protein expression was induced using L-arabinose and IPTG at final concentrations of 0.2 % (w/v) and 1 mM, respectively, and allowed to grow for a further three hours. Then, the bacterial cells were harvested by centrifugation at 4,248 x g. Following this, the obtained pellet was resuspended in ice-cold Buffer A (25 mM Tris-HCL pH 7.5, 5 mM $MgCl_2$, 1 mM PMSF, EDTA-free protease inhibitor cocktail tablet (1 tablet for 0.5 mL), and 100 µg/mL DNase I). Next, the cells in the suspension were lysed using a French pressure cell press (Polytec, Germany) at 1200 psi and centrifuged at 38,759 x g for one hour at 4° C. As expected [18], the expressed HCC was enriched in inclusion bodies and, therefore, the pellet was further processed. The pellet was resuspended in Buffer B (20 mM Tris-HCL pH 8, 500 mM NaCl, 6 M urea, 10 mM β-mercaptoethanol and 0.1 % (w/v) DDM) and sonicated for homogenization. The homogenate was subjected to centrifugation. All centrifugation steps were performed using Sorvall Lynx 4000 centrifuge (Thermo scientific, Waltham, MA, USA). Cell harvesting was performed using a F12-6x500 LEX rotor (Thermo scientific, Waltham, MA, USA) and the remaining centrifugation steps for protein separation were performed using a A27-8x50 rotor (Thermo scientific, Waltham, MA, USA).
The filtered supernatant was loaded over a Ni-NTA-agarose column (Qiagen, Germany) and purified using an FPLC system (Biorad NGC chromatography system, Hercules, California, USA) following the manufacturer's protocol. All purified fractions were screened by SDS-PAGE (15 % resolving gel) and Coomassie Blue staining. The fractions consisting of HCC (~18 kDa) were isolated and further purified by reverse-phase HPLC

138 (Shimadzu, Japan) using a VYDAC 10 µm C8 column (250 x 4.6 mm) equipped with a 208TP Aquapore
139 guard cartridge (Avantor, Pennsylvania, USA). A linear gradient of acetonitrile in 10% trifluoroacetic acid was
140 used as the mobile phase. All fractions were monitored at 280 nm with an integrated UV-visible detector. The
141 main absorption peaks were screened by SDS-PAGE and silver staining. DDM was added (0.1 % (w/v) for 1
142 mg/mL protein) to the HCC containing fractions for protein stabilization. Finally, the HCC containing
143 fractions were lyophilized and stored at -20 °C until any further use. Unless mentioned, the lyophilized protein
144 fractions were resuspended in ice cold 20 mM NaP buffer (pH 7.4) when needed. For fluorescence microscopy
145 experiments, protein labelling was performed using the primary amine reactive dye Alexa Fluor® 488 (AF488)
146 following the manufacturer's protocol. In this regard, a degree of labelling (*DOL*) ~0.2 was reached, as
147 confirmed via optical spectroscopy measurements (data not shown).
148 Only a minor modification to the protocol was needed for the HCC mutant Δ68 [45] , which was purified from
149 the soluble fraction of the bacterial lysate using urea free buffer and labelled following the same protocol.
150
151
152 *3. PIP strip™ blotting*
153
154 PIP strips™ (ThermoFisher Scientific, catalog no. P23751, Waltham, MA, USA) were used for screening the
155 PL binding preference of the purified HCC according to a published protocol [46]. For blocking unspecific
156 interactions, each membrane was incubated in Buffer C (137 mM NaCl, 2.7 mM KCl, 19mM Tris base, 0.1 %
157 (v/v) Tween®20) + 1 % (w/v) skim milk (blocking buffer) for one hour at room temperature (RT).
158 Subsequently, the blocked strip was incubated overnight with 1 µg/mL unlabelled HCC in 20mM NaP buffer
159 at 4 °C. The incubated strip was then washed three times with Buffer C and subjected to one hour incubation
160 with mouse anti-HCV Core antibody (ThermoFisher Scientific, catalog no. MA1-080, Waltham, MA, USA)
161 in blocking buffer (1/1000 dilution). The washing step was then repeated, followed by the addition of goat
162 anti-mouse alkaline phosphatase (AP) conjugated secondary antibody (Invitrogen, catalog no. 31320,
163 Waltham, MA, USA) (1/5000 dilution). After one hour incubation with the secondary antibody, the washing
164 step was repeated, and the membrane was treated with the AP substrate kit (BioRad, catalog no. 1706432,
165 Hercules, California, USA) for chromogenic detection of possible protein binding to the PL spots using the
166 manufacturer's protocol. Images of the developed membrane were acquired using an image scanner
167 (ImageScanner III, GE, Boston, MA, USA). Quantification of protein binding intensities was performed using
168 Fiji software [47].
169
170
171
172
173

174 *4. Preparation of ALDs*
175
176 ALDs were employed as *in vitro* lipid monolayer platforms for the quantitative investigation of HCC-lipid
177 interaction. ALDs were prepared using triolein as the oil phase according to an available protocol [48] with slight
178 modifications [39]. Firstly, a PL solution mixed with 0.001 molar% (w/v) Rh-PE (or 0.005 molar% TF-PC) in
179 methanol was dried in a microcentrifuge tube under a nitrogen stream. The dried film was dispersed in pre-
180 warmed triolein (1/1000 mass ratio) and the mixture was extensively vortexed for 15 minutes and bath
181 sonicated for 30 minutes. Throughout the manuscript, triolein is referred to as "oil". The solution was then
182 added to 20 mM NaP buffer of pH 7.4 (1:10 v/v) and sonicated for ten seconds after short mixing, thus
183 obtaining a milky white oil-in-buffer emulsion which contained the ALDs. 75 µL of this ALD emulsion was
184 transferred to an observation chamber, which was diluted with an equal volume of the same buffer before
185 imaging. This procedure results in ALDs with monolayer mean molecular area (*MMA*) or area per PL values
186 roughly comparable to cellular or physiological LDs (i.e., ~80 $Å^2$/lipid, also referred to as *pMMA*) [49,50], as
187 quantified via lsFCS (see below). To obtain three more different *MMA* values, the PL to oil mass ratio was
188 adjusted accordingly, e.g. 1/2000 PL/oil mass ratio for an increase in *MMA* as compared to *pMMA*, or 1/500
189 and 1/250 PL/oil mass ratios for a decrease in the *MMA* values. When needed, β-mercaptoethanol was mixed
190 to this solution to a 5 % (v/v) final concentration for experiments in reducing environment. Next, AF488-
191 labelled HCC was mixed to a final concentration of 200 nM and incubated for two hours. For Δ68, the final
192 concentration was 500 nM. In the case of experiments conducted to compare the multimerization of Δ68 and
193 HCC on the PL monolayer (i.e for experiments in which comparable binding to the ALD is needed for the
194 two proteins), the latter was added to a final concentration of ~20 nM. Following the incubation step, the
195 sample with the protein-ALD suspension was washed with 20 mM NaP to get rid of the unbound protein
196 molecules.
197
198
199 *5. Preparation of GUVs*
200
201 GUVs as model of the ER bilayer [33] were used to investigate the binding behaviour of HCC to PLs. To
202 highlight and compare the role of specific anionic PL, GUVs were prepared with the same PL compositions
203 as ALDs by electroformation, using cylindrical Teflon chambers containing two platinum wires [51,52] following
204 an available protocol [39]. PL solutions (2.5 mg/mL) were mixed with 0.005 molar% Rh-PE and 1 molar%
205 biotinylated-PE. Following the electroformation, 100 µL of GUV suspension were transferred to an
206 observation chamber, which was pre-treated with 100 µg/ml Streptavidin for 12 hours and then 10 % (w/v)
207 BSA solution for 15 minutes. This suspension was further diluted with an equal volume of 40 mM NaP buffer
208 and the GUVs were then allowed to settle down for 30 minutes, allowing the binding to the bottom of the

plate. Next, AF488-labelled HCC was mixed to a final concentration of 200 nM and incubated for 2 hours. Finally, the GUVs were washed with 40 mM NaP to remove the unbound protein.

6. Line-Scan fluorescence correlation spectroscopy

Fluorescently labelled HCC binding, multimerization state and dynamics on ALDs and GUVs were quantified in terms of fluorescence intensity, brightness and diffusion coefficient ($D_{Protein}$), respectively, using lsFCS. Furthermore, the same approach was used to measure PL diffusion coefficient (D_{PL} or $D_{PL/TF\text{-}PC}$) and packing density (indicated by the *MMA*) in ALD monolayers labelled with 0.001 molar% Rh-PE (or 0.005 molar% TF-PC).

LsFCS was performed on GUVs and LDs based on previous protocols [39,53]. Briefly, membranes were scanned perpendicularly with a pixel dwell time of 0.67 µs (pixel size 0.08 µm) at resolution of 256 pixels (total scan time ~4 min). Large-scale (ca. > 1µm) PL or protein cluster sites on the membrane were avoided in order to scan a relatively homogenous region. Importantly, unless a cluster was encountered, scanning was always performed at the lower right side of the membrane (135°) of each ALD or GUV.

All images were acquired with a Zeiss LSM880 system (Carl Zeiss, Oberkochen, Germany) using a Plan-Apochromat 40x/1.2 Korr DIC M27 water immersion objective and a 32-channel gallium arsenide phosphide (GaAsP) detector array. AF488-labelled HCC bound to ALD or GUV surface were imaged using a 488 nm Argon laser (0.77 µW at the exit of the objective). Analogous experiments in samples without proteins were performed to determine *MMA* and D_{PL} in ALDs, using a 561 nm diode laser (1.97 µW). For measurements in the presence of HCC, D_{PL} was determined simultaneously with the protein measurement on the same ALD, while for $D_{PL/TF\text{-}PC}$ determination, unlabelled HCC was used. For all measurements, the photobleaching and the background were kept below ca. 10 % and 1% of the total initial intensity, respectively [39].

Prior to performing lsFCS, calibration of the excitation beam waist (w_0) was performed each day by measuring the fluorescence autocorrelation curve of 0.25 µM AF488 in 20 mM NaP to correct the laser alignment variation. This calibration procedure was also performed for the PL (Rh-PE) experiments, using a similar concentration of Alexa Fluor® 555 (ThermoFisher Scientific, Waltham, MA, USA) (AF555) dye. Next, a mean of the diffusion times (τ_{Diff}) from three independent autocorrelation curves was used to calculate w_0 by applying the reported diffusion coefficient (D) of the fluorescent dyes [54,55] following **Equation 1**:

$$D = \frac{w_0^2}{4 \cdot \tau_{Diff}} \qquad (1)$$

As an approximation, the ca. 2 % decrease in D due to the presence of the solute [56,57] was neglected [39]. Each data set was analysed as mentioned in previous work [39].

The effective illuminated area (A_{eff}) on the GUV or ALD was estimated as [40]:

$$A_{eff} = \pi \cdot S \cdot w_0^2 \qquad (2)$$

wherein the structural parameter is denoted by S (derived as mentioned in previous work [39]).
The analysis of each measurement resulted in the number of particles (N) in the measured area, the integrated line intensity (I) and τ_{Diff} for the fluorophore (AF488 labelled HCC/ Rh-PE/ TF-PC). I was calculated as the time integral of the fluorescence signal in the immediate proximity of the membrane [58,59] and expressed in Hz. For the PL-only experiments, the total number of PL molecules in the illuminated area (N_{total}) was determined, which was used to calculate the PL *MMA* on the ALD surface [39]:

$$MMA = \frac{A_{eff}}{N_{total}} \qquad (3)$$

For the measurements with AF488 labelled HCC, the measured I was normalized through i) the brightness value of AF488 (B_{dye}) obtained from daily calibration in solution (so to avoid errors caused by changes in laser power or optics alignment) and ii) the degree of labelling of the protein (so to correct for small sample-to-sample variations). In this regard, the typical *DOL* was ca. 0.2.
Protein brightness ($B_{Protein}$) was determined as [60]:

$$B = \frac{I}{N} \qquad (4)$$

Hence, $B_{Protein}$ was expressed in Hz/molecule (Hz/mol) according to **Equation 4**.

The I and $B_{Protein}$ values were converted into protein monomer concentration (mol/µm^2) and multimerization state, respectively. In this context, the number of protein monomers in the detection area was calculated by dividing the respective I value by the monomer brightness ($B_{monomer}$: in a rough approximation, the lowest $B_{Protein}$ value of all measurements). Next, the protein concentration was obtained by dividing the number of protein molecules by the A_{eff}. Finally, the total number of bound proteins was obtained by dividing the labelled protein concentration by the *DOL*. Hence:

$$Protein\ Concentration = \frac{\left(I/B_{monomer}\right)}{A_{eff} \cdot DOL} \qquad (5)$$

Following this, the multimerization state from each brightness value was calculated based on the reported equation [60]:

$$Multimerization\ state = 1 + \frac{\left({B_{Protein}}/{B_{monomer}}\right)-1}{DOL} \qquad (6)$$

7. Image correlation spectroscopy

Image correlation spectroscopy (ICS) was performed on confocal images of ALDs and GUVs acquired with the above-described setup. Image acquisition was performed with a pixel dwell time of 2.06 µs and a resolution of 1024 X 1024 pixels (pixel size 0.02 µm). A "donut"-shape selection was first performed around the ALD or GUV membrane with Fiji software [61] and only round shaped ALDs were analysed. Next, this selection was linearized into a rectangular image (with the *x*-coordinate describing the length of the membrane) using a Fiji script (Ves_unwrapper.ijm) [61]. Then, this image was further analysed using a custom-written MATLAB code. Briefly, the image was integrated along the *y*-coordinate to generate the spatial variations in the fluorescence intensity along the membrane circumference in the form of a one-dimensional profile. Next, a one-dimensional autocorrelation function was calculated and a fit with a Gaussian model was performed. The amplitude of this fitted curve (*a*) is inversely proportional to the cluster density [42]. The average intensity per cluster, referred to as the degree of clustering (*DOC*), was calculated as the product of the average fluorescence intensity of the entire ALD or GUV circumference and the obtained parameter *a*. Finally, the *DOC* value was normalized through the same procedure as for *I* (see last paragraph).

8. Software

Statistical significance of differences between data sets were calculated using one-way ANOVA (significance level=0.05). All figures and statistical tests were made using Origin Pro 2023 (OriginLab Corporation, Northampton, MA, USA) [38,39]. Fluorescence microscopy images were processed using Fiji software. All data were analysed with Matlab 2020b (The MathWorks, Natick, MA, USA) using already available codes [39]. Primer designing was performed using Benchling (San Francisco, California, USA).

Results

1. Anionic PLs in LDs promote binding and multimerization of HCC

HCV infection is associated to an increase in intracellular concentration of certain anionic PLs, such as PI(4)P and PI(4,5)P2 [8,34,36]. However, it is not known whether these PLs play a role in HCC interactions with monolayers or bilayers. In order to understand the PL binding behaviour of HCC, we performed first a preliminary screening using immobilized PLs (i.e., PIP™ strips). PLs carrying different headgroups are presented on a nitrocellulose membrane and patterned as separate spots to qualitatively test protein-PL interactions. Following this procedure, HCC binding was detected mostly within anionic PL spots with varying intensities, depending on the PL headgroup (**Figures 1A** and **S1**). The highest binding signal was observed for PI(4)P and PI(3)P, while that for the zwitterionic PL, PC was among the weakest signals that could still be quantified (**Figure S1**). The results were reproducible, except for PI(3,4,5)P3, PI(3,4)P2, PI and PE PLs which were, therefore, not further investigated. For the following experiments, we thus focused on PI(4)P (as example of phosphoinositide with one phosphate group strongly interacting with HCC), PI(4,5)P2 (as example of phosphoinositide with two phosphate groups also interacting with HCC), PS (as an example of a non-phosphoinositide anionic PL still showing an interaction with HCC) and PC (as a negative control), as summarized in **Figure 1B**.

We proceeded to investigate HCC-lipid interactions directly in biophysical models of LDs by means of confocal microscopy and lsFCS. The latter measures the fluctuations in fluorescence emission from a spatially confined region of the membrane (see **Methods**) and calculates the labelled molecule mobility (in terms of D values), local abundance (in terms of the measured fluorescence signal I and the detected number of particles N) and multimerization state (in terms of brightness values) [40,62].

First, we characterized protein-free ALDs to determine typical *MMA* values and the corresponding PL dynamics. By using multiple PL/oil mass ratios (see **Methods**), it is possible to cover an *MMA* range between ca. 40 and 120 Å²/PL (**Figure S2** and **Table S5**). PL mobility was quantified as a function of *MMA*, to confirm that the monolayer dynamics in our ALD model vary as expected [39,63]. Specifically, D_{PL} values range from ~5 µm²/s to ~9 µm²/s (~6 µm²/s for phosphatidylinositol PLs) for increasing *MMA* values, as expected for unsaturated PLs at the oil-water interface [64] (**Figure S2**). Also, we could identify the best PL/oil ratios needed for each PL composition to obtain *MMA* values either in the range 75-85 Å²/PL, i.e. *pMMA* [49,50] or in the range 40-50 Å²/PL (i.e., an arbitrarily chosen range, here defined as "low *MMA*"), as shown in **Table S5**. This estimation procedure is needed later for samples containing proteins, in which the *MMA* of each ALD cannot be directly measured (due to protein-lipid interactions, see below). For example, to obtain *pMMA* samples, a PL/oil mass ratio of 1:1000 is required for DOPC ALDs, while 1:500 is more suitable for DOPC + PI(4)P (9:1) ALDs.

346 Next, we analysed HCC binding by quantifying the fluorescence signal of AF488-labelled HCC bound to PL
347 monolayers formed at *pMMA*. For ALDs composed of the zwitterionic PL DOPC, the addition of small amount
348 (i.e., 10 mol%) anionic PLs has only a minor effect on HCC binding (**Figure 1C**). Of note, control experiments
349 with fluorescent PL analogues suggest that the different anionic PLs tested here partition into the monolayer
350 in the expected amounts (**Figure S3**). Interestingly, the protein associates to the surface of ALDs even more
351 efficiently if no PLs are present ("No PL" condition). For ALDs prepared from pure DOPC, "low *MMA*"
352 values (i.e. higher PL density) are associated to a ca. 50% decrease in protein binding (cf. **Figures 1C** and **D**,
353 **Figure S4**), as expected from previous reports [33]. Interestingly, this effect is much less evident for ALDs
354 containing 10 mol% DOPS (ca. 25% decrease) or PI(4)P (no decrease). Strikingly, **Figure S4** shows that
355 protein binding even increases at higher PL packing density in ALD monolayers containing PI(4,5)P2,
356 compared with the same ALDs at *pMMA*. **Figure 1E** shows typical confocal microscopy images of the
357 examined ALDs at *pMMA*, in which the green channel indicates the AF488-labelled protein signal, and the
358 red channel indicates the fluorescent PL signal (0.001 molar% Rh-PE). In line with lsFCS quantification
359 (**Figure 1C**), HCC appears to bind efficiently to ALDs in the absence of PLs and much less when PLs form a
360 monolayer at the surface of the ALD (note the different colour scaling for DOPC, DOPS and PI(4)P, as
361 indicated in the caption). A similar trend and a general agreement between confocal imaging and lsFCS is
362 observed also at "low *MMA*" values/ high PL packing (**Figure S5**). Microscopy imaging additionally indicates
363 that the lateral distribution of PLs and HCC is not homogeneous, especially in the presence of anionic PLs.
364 Further analysis of HCC-ALD interactions via lsFCS indicates that the average protein multimerization
365 (quantified via molecular brightness, see **Methods**) does not strongly depend on the tested PL compositions,
366 at least at *pMMA* (**Figure S6A**). At higher PL packing or "low *MMA*", enhanced multimerization is observed
367 e.g. for ALDs containing 10 mol% PI(4)P compared to 10 mol% DOPS (**Figure S6B**) but, in general, a simple
368 correlation of protein multimerization with *MMA* or PL identity is not evident over all the tested *MMA* values
369 (**Figure S6C**). On the other hand, a clearer trend is observed when plotting HCC multimerization as a function
370 of local protein concentration (i.e., protein fluorescence intensity) (**Figure S7A**). The observed molecular
371 brightness values range from ~0.2 KHz/mol at low protein concentration to ~1 KHz/mol at the highest protein
372 concentration measured, depending on PL composition. Considering that the protein labelling efficiency was
373 ~0.2 dye molecules/protein and assuming that the lowest brightness we measured during this study (i.e. ~0.1
374 KHz/mol in GUVs, see below) corresponds to HCC monomers, it is possible to roughly estimate that HCC
375 forms multimers with up to ca. 50 subunits at concentrations ~1600 monomers/μm^2 (**Figure S7B**) in the
376 presence of PI(4)P. For DOPS and PI(4,5)P2 this number was 20-35 subunits. Interestingly, such
377 concentration-dependent multimerization is less evident for pure DOPC LDs. Next, an empirical model [65] was
378 fit to the data in **Figure S7B** and the results confirm that the multimerization is the most efficient in LDs
379 containing PI(4)P, while no significant difference can be observed for LDs containing DOPC, DOPS or
380 PI(4,5)P2 (**Table S6 v**).

Finally, we analysed the diffusive dynamics of HCC in ALDs under the investigated conditions (**Figures S7C** and **S8**). $D_{Protein}$ ranges from ~0.4 to ~1 µm²/s, with no strong correlation to protein concentration (**Figure S7C**), PL type (**Figures S8A** and **B**) or PL packing (**Figure S8C**).

In conclusion, these results indicate that negatively charged PLs promote HCC binding to LDs, if PLs are tightly packed within the monolayer. Furthermore, PI(4)P appears to enhance HCC concentration-dependent multimerization behaviour.

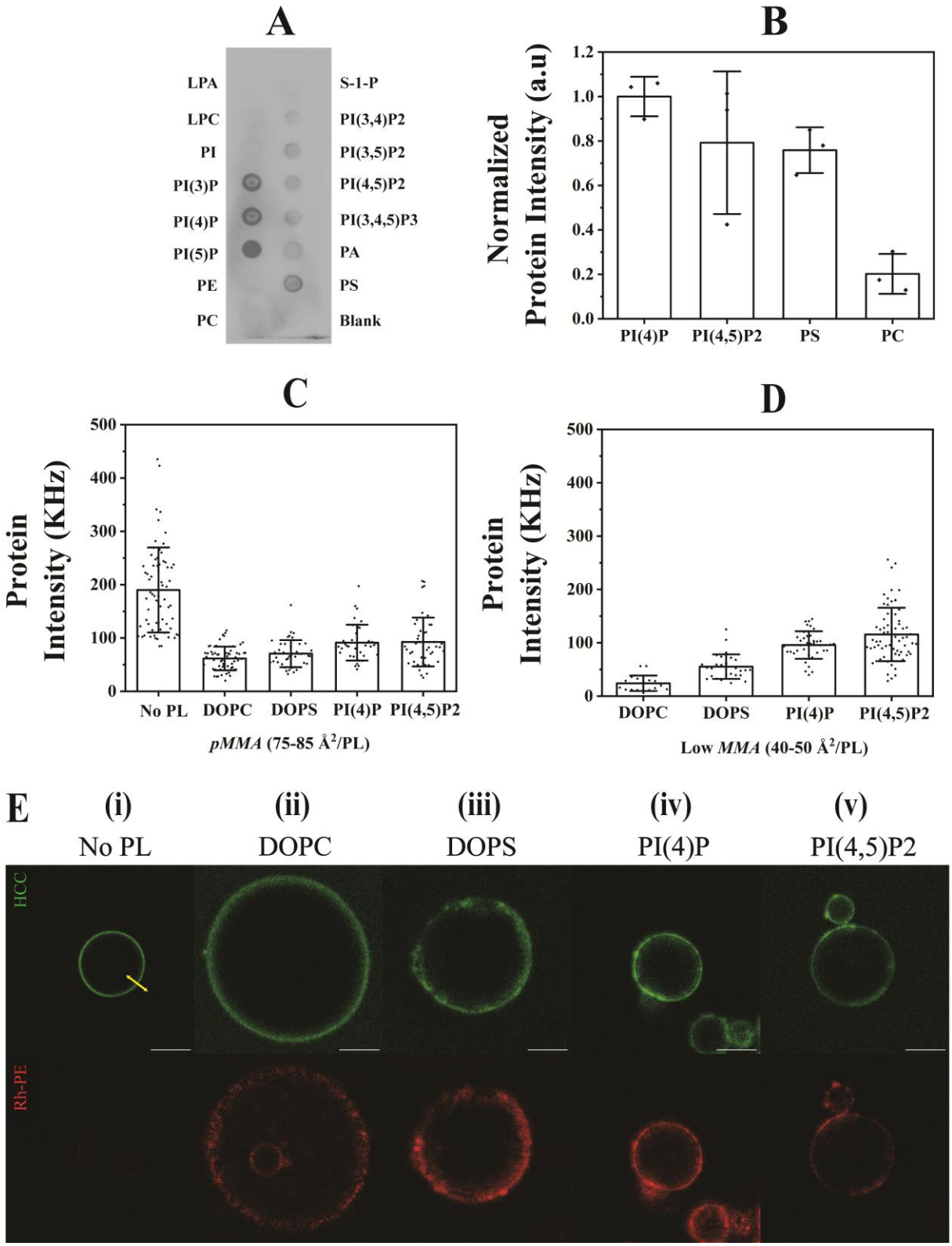

Figure 1: HCC binding to ALD monolayers depends on PL identity.
A shows a typical binding pattern of HCC to different lipids in a PIP™ strip detected using complementary antibodies. **B** shows the quantification of HCC binding intensity to each spot from three independent experiments for four selected PLs. All data are normalized relative to PI(4)P. **C** and **D** show the quantification of AF488-labelled HCC binding to ALDs performed via lsFCS and are represented as mean fluorescence intensity measured within the scanned region of the membrane (see Methods). **C** and **D** show the protein fluorescence intensity for ALD monolayers at *pMMA* and "low *MMA"* conditions, respectively. *MMA* values were not directly measured but rather estimated from protein-free ALDs prepared with the same PL/oil ratios and (see **Table S5**). The LDs are distinguished based on the interface PL composition: "No PL" refers to ALDs composed of only oil, "DOPC" to ALD monolayer composed of pure DOPC, "DOPS" to ALD monolayer composed of DOPC+DOPS (9:1 molar ratio), "PI(4)P" to ALD monolayer composed of DOPC+PI(4)P (9:1 molar ratio) and PI(4,5)P2 to ALD monolayer composed of DOPC+PI(4,5)P2 (9:1 molar ratio). All bars represent mean values with whiskers as the SD. Each point represents the result of one lsFCS measurement within one ALD. The points are pooled from at least three independent experiments. See **Tables S1**, **S2** and **S3** for details on statistics. **E** shows representative fluorescence images of HCC-ALD interaction, in connection to **C**. For each column, for the same samples shown in panel **C**, the green channel (top) represents AF488-labelled HCC, and the red channel (bottom) represents Rh-PE doped (0.001 molar%) ALDs. The yellow line in **(i)** depicts a typical scanning line used for lsFCS. The colour intensity range in the green channel for **(ii)**, **(iii)**, **(iv)** and **(v)** was reduced by a factor of 4.5 with respect to that of **(i)** using Fiji software, for better visualization. Scale bar is 5 µm.

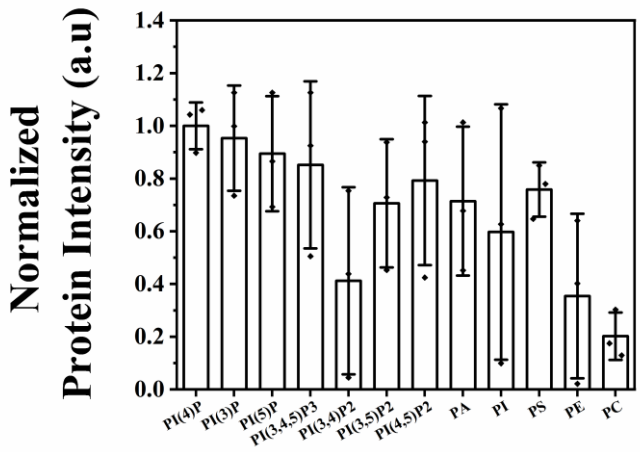

Figure S1: Normalized HCC binding intensity within lipid spots of PIP™ strip.
HCC binding to each PL spots on the PIP™ strip (**Figure 1A**) shown after normalization to the PI(4)P value. Protein binding signal was obtained from the chromogenic detection of a complementary antibody (see **Methods**). Bars represent mean values with whiskers as the SD. Data points were obtained from three independent experiments. See **Table S1** for details on statistics.

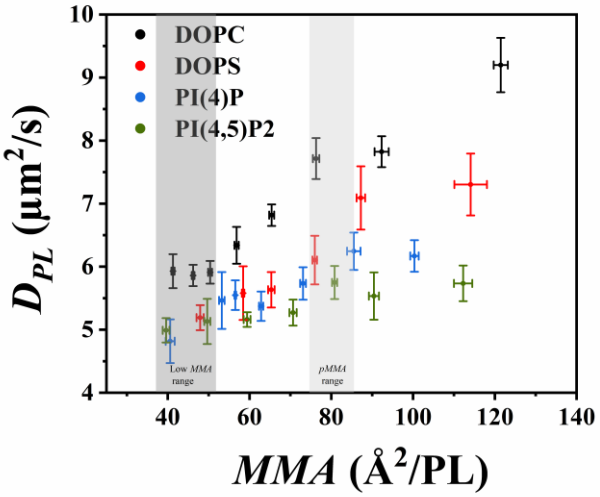

Figure S2: PL mobility in protein-free ALDs increases as a function of decreasing packing density.
PL mobility and packing density represented as D_{PL} and *MMA* respectively, were obtained via lsFCS analysis [39]. All monolayers were doped with 0.001 molar% Rh-PE. D_{PL} is plotted as a function of *MMA*. For each PL, ALD monolayers with 4 different estimated *MMA*s were produced by adjusting the PL/oil ratio (see **Methods**). For better visualization, data points were binned so that each point represents the mean value calculated from 13-29 experimental points for DOPC ALDs, 12-37 points for DOPS-containing ALDs, 9-19 points for PI(4)P-containing ALDs and 13-20 points for PI(4,5)P2-containing ALDs. Light grey and dark grey boxes show the *pMMA* range and "low *MMA*" range respectively. Each colour represents the parameters obtained from ALD monolayers formed of DOPC, DOPC+DOPS (9:1), DOPC+PI(4)P (9:1) and DOPC+PI(4,5)P2 (9:1). Error bars are SEM.

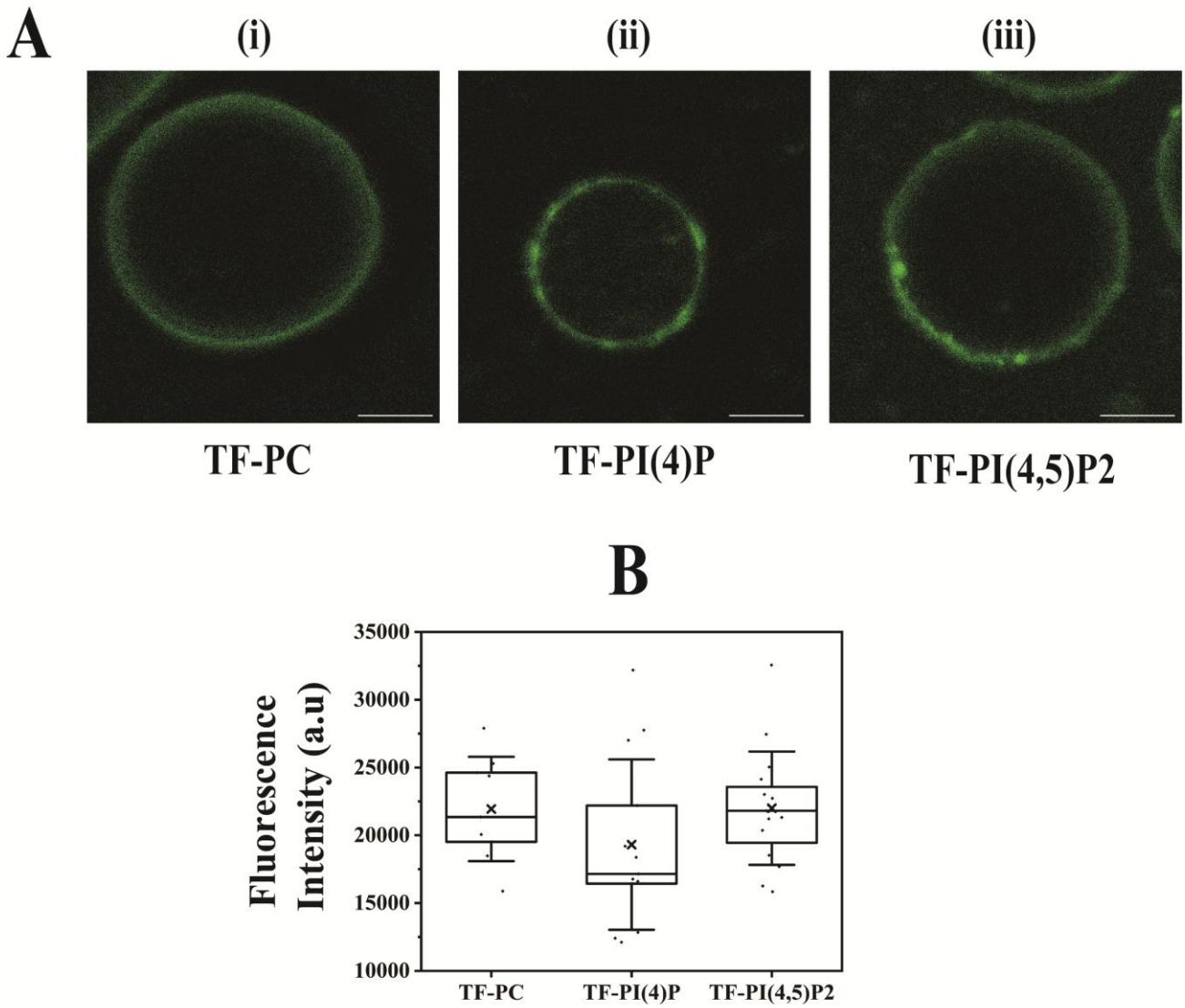

Figure S3: Inclusion of different (charged) PLs into LDs is not strongly affected by PL identity.
A shows typical fluorescence images of ALD monolayers under *pMMA* conditions labelled with TopFluor® -PC (TF-PC) **(i)**, TF-PI(4)P **(ii)** and TF-PI(4,5)P2 **(iii)**. All monolayers were composed of DOPC and 0.005 molar% of the respective fluorophore. The colour intensity range was reduced by a factor of 4.5 with respect to that of **Figure 1E (i)** (green channel) using Fiji software, for better visualization. Scale bar is 5 µm. **B** shows the distribution of monolayer fluorescence intensity values of at least 9 ALDs of each fluorophore type i.e. TF-PC, TF-PI(4)P or TF-PI(4,5)P2 represented in the form of box plots. Fluorescence intensities were quantified using Fiji software [61] and Matlab. In all box plots, the horizontal line represents the median value, while the 'x' indicates the mean with the first and third quartile as the boundaries. The whiskers indicate SDs. Both zwitterionic and anionic TopFluor® derivatives partition in the ALD monolayer as expected, as shown by the similar fluorescence intensities in **B** (determined via one-way ANOVA, $p > 0.05$). See **Table S5(i)** for the data points.

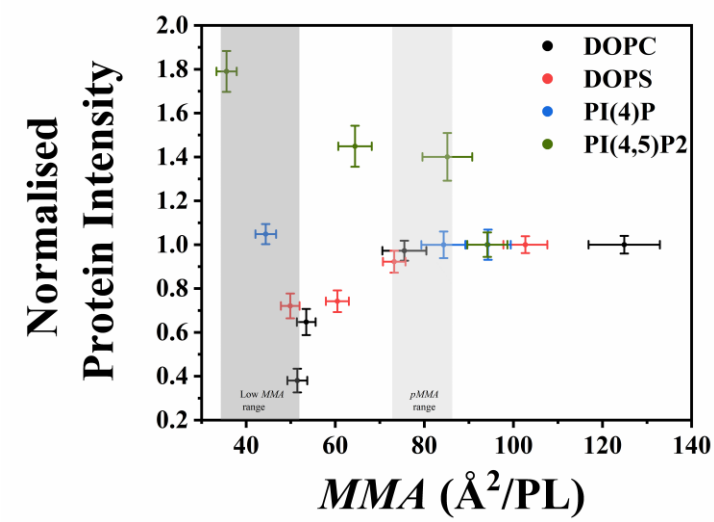

Figure S4: Interplay between HCC binding and monolayer *MMA* is determined by PL composition. Quantification of AF488-labelled HCC binding to LDs composed of DOPC, DOPC+DOPS (9:1), DOPC+PI(4)P (9:1) and DOPC+PI(4,5)P2 (9:1) was performed via lsFCS and represented as fluorescent protein intensity. The normalized values are represented as a function of ALD monolayer *MMA*, which, in turn, were determined for 4 PL/oil ratios and measured via lsFCS (see **Methods** and **Table S5**). Here, each point represents the mean values of each of the two parameters obtained from at least 18-59 experimental points for DOPC ALDs, 28-51 points for DOPS mixed ALDs, 37-40 points for PI(4)P mixed ALDs and 38-69 points for PI(4,5)P2 mixed ALDs with error bars as SEM. *MMA* values were not directly measured but rather estimated from protein-free ALDs prepared with the same PL/oil ratios (see **Table S5**). Light grey and dark grey boxes show the *pMMA* range and "low *MMA*" range respectively. All monolayers were labelled with 0.001 molar% Rh-PE. See **Table S5** for details on the statistics.

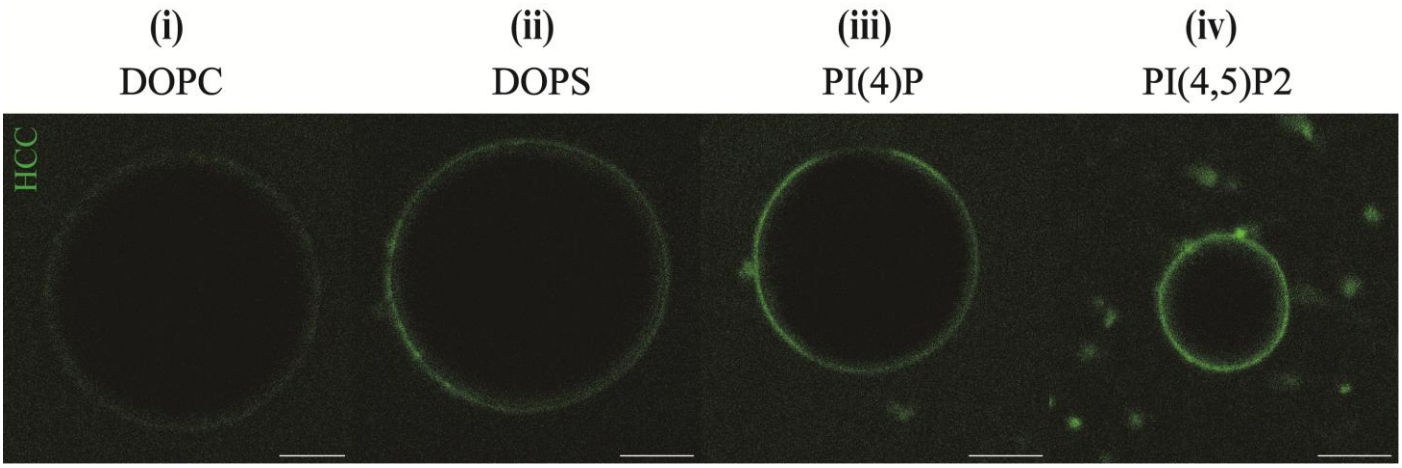

Figure S5: HCC binding to ALD monolayers with high PL packing depends on lipid identity. **(i)-(iv)** show representative fluorescence images of AF488-labelled HCC binding to ALD monolayers with "low *MMA*" (i.e., 40-50 Å²/PL), composed of DOPC, DOPC+DOPS (9:1), DOPC+PI(4)P (9:1) and DOPC+PI(4,5)P2 (9:1) respectively. These images exemplify the results shown in **Figure 1D**. To enhance visibility, the colour intensity range in all the images was reduced by a factor of 4.5 with respect to that of **Figure 1E (i)** (green channel). Scale bar is 5 µm.

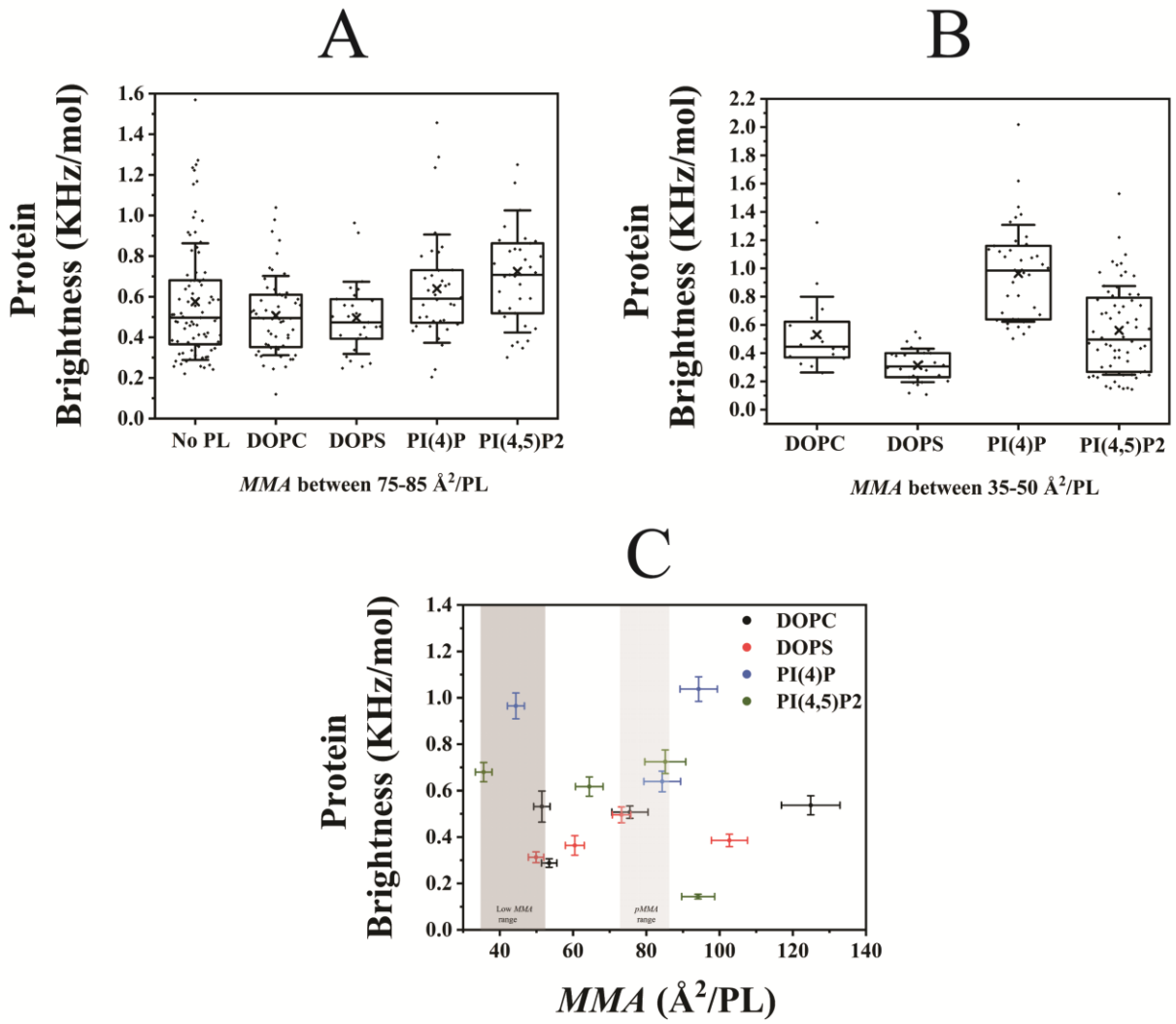

Figure S6: HCC multimerization depends only weakly on ALD monolayer composition and *MMA*. Quantification of AF488-labelled HCC multimerization via lsFCS-based brightness analysis for the same ALD monolayers as in **Figures 1C**, **D** or **S4**. **A** and **B** show the HCC brightness values for proteins binding to different ALD monolayers at *pMMA* and "low *MMA*", respectively, as box plots. The ALD monolayers are composed of DOPC, DOPC+DOPS (9:1), DOPC+PI(4)P (9:1) and DOPC+PI(4,5)P2 (9:1). **A** shows additionally the brightness data for ALDs made only of oil, i.e. bare oil droplets. Each point represents the result of one lsFCS measurement within one ALD. In all box plots, the horizontal line represents the median value, while the 'x' indicates the mean with the first and third quartile as the boundaries. The whiskers indicate SDs. Data points were pooled from at least 3 independent experiments. **C** shows the protein brightness values as a function of ALD monolayer *MMA*. *MMA* values were not directly measured but rather estimated from protein-free ALDs prepared in the same conditions, as indicated in **Table S5**. Light grey and dark grey boxes show the *pMMA* range and "low *MMA*" range, respectively. Here, each point represents the mean values of each of the two parameters obtained from at least 16-54 experimental points for DOPC ALDs, 26-36 points for DOPS mixed ALDs, 35-38 points for PI(4)P mixed ALDs and 32-64 points for PI(4,5)P2 mixed ALDs with error bars as SEM. ALD monolayers were labelled with 0.001 molar% Rh-PE. See **Tables S2**, **S3** and **S5** for the details on the statistics.

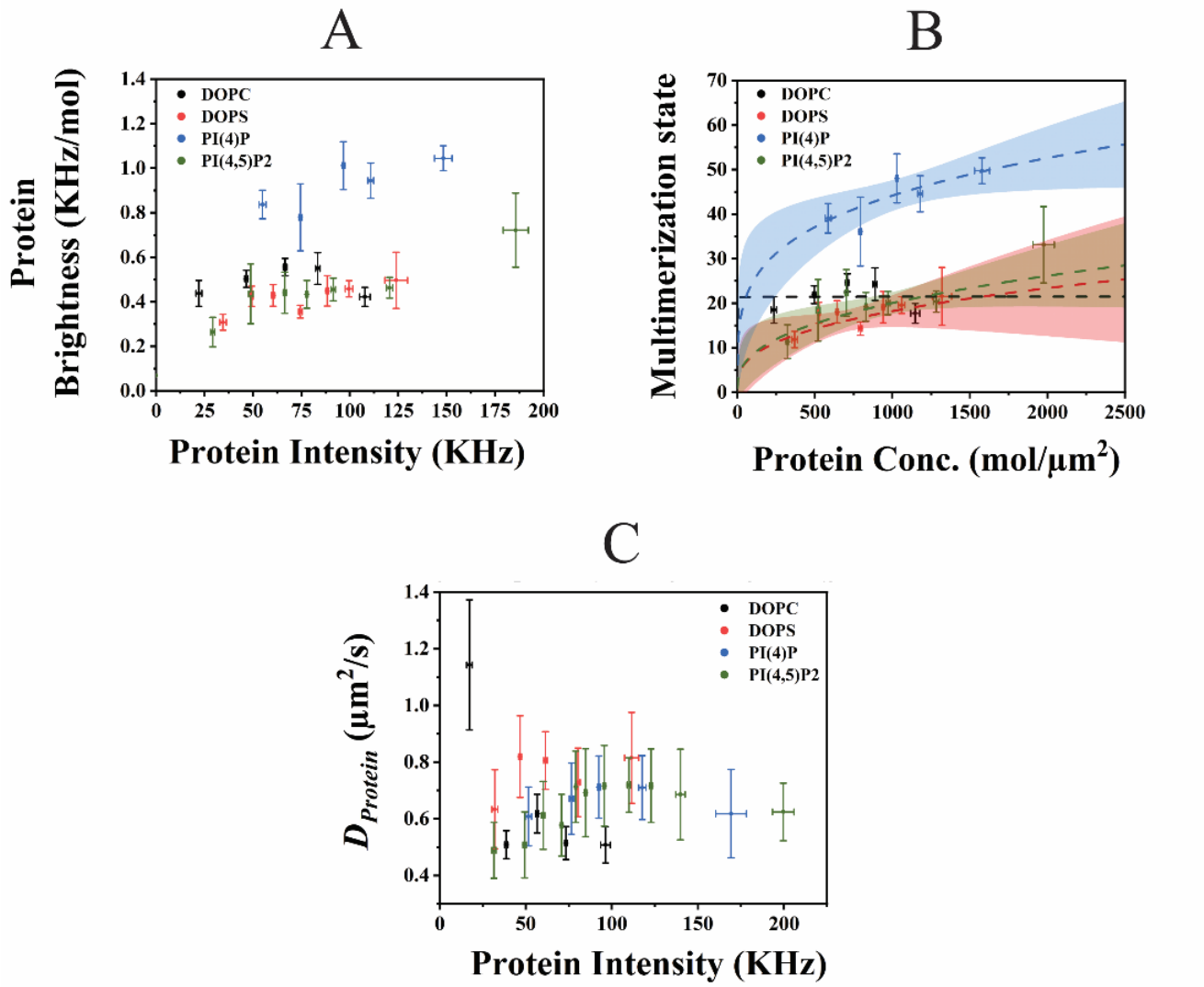

Figure S7: HCC multimerization and mobility as a function of HCC concentration on LDs.
HCC multimerization, mobility and binding on LD monolayers composed of different PLs are quantified via the parameters: protein brightness (or multimerization state), $D_{Protein}$ and fluorescence protein intensity (or protein concentration), respectively. These parameters were obtained via lsFCS analysis of the same LDs as in **Figures S4** and **S6C**. **A** shows the protein brightness values for each LD composition plotted as a function of the corresponding protein fluorescence intensity values. Each colour indicates the parameters measured on LD monolayers made of DOPC, DOPC+DOPS (9:1), DOPC+PI(4)P (9:1) and DOPC+PI(4,5)P2 (9:1). For better visualization, the data points were binned so that each point represents the mean value calculated from 9-43 points for DOPC LDs, 10-28 points for DOPS mixed LDs, 7-30 points for PI(4)P mixed LDs and 13-37 points for PI(4,5)P2 mixed LDs. **B** shows the multimerization state values (via **Equation 6**) plotted against the corresponding protein concentration (via **Equation 5**). The data points correspond to those shown in **A**, with the same colour code. The dashed lines show the best fit to the experimental data points, using the empirical model *y=ax^b+1* [65]. 95% confidence interval range for each fit is shown by the respective colour bands. The data for DOPC were not fitted with the same model and, instead, only their average is shown as a dashed horizontal black line (i.e., *b* fixed to 0). The *a* value for PI(4)P mixed ALDs is significantly higher than that for DOPS and PI(4,5)P2 mixed ALDs ($p<0.001$), as determined via one-way ANOVA. The *a* value difference between DOPS and PI(4,5)P2 mixed ALDs is not significant ($p>0.05$). **C** shows the protein diffusion coefficients $D_{Protein}$ for each LD composition as a function of the respective protein intensity values. As for **A**, data point binning was performed such that each point represents the mean value calculated from 18-37 points for DOPC LDs, 15-32 points for DOPS mixed LDs, 13-35 points for PI(4)P mixed LDs and 9-19 points for PI(4,5)P2 mixed LDs. The error bars in all figures represent the SEM calculated from the binning procedure. See **Table S6** for the details on the data points and fit parameters.

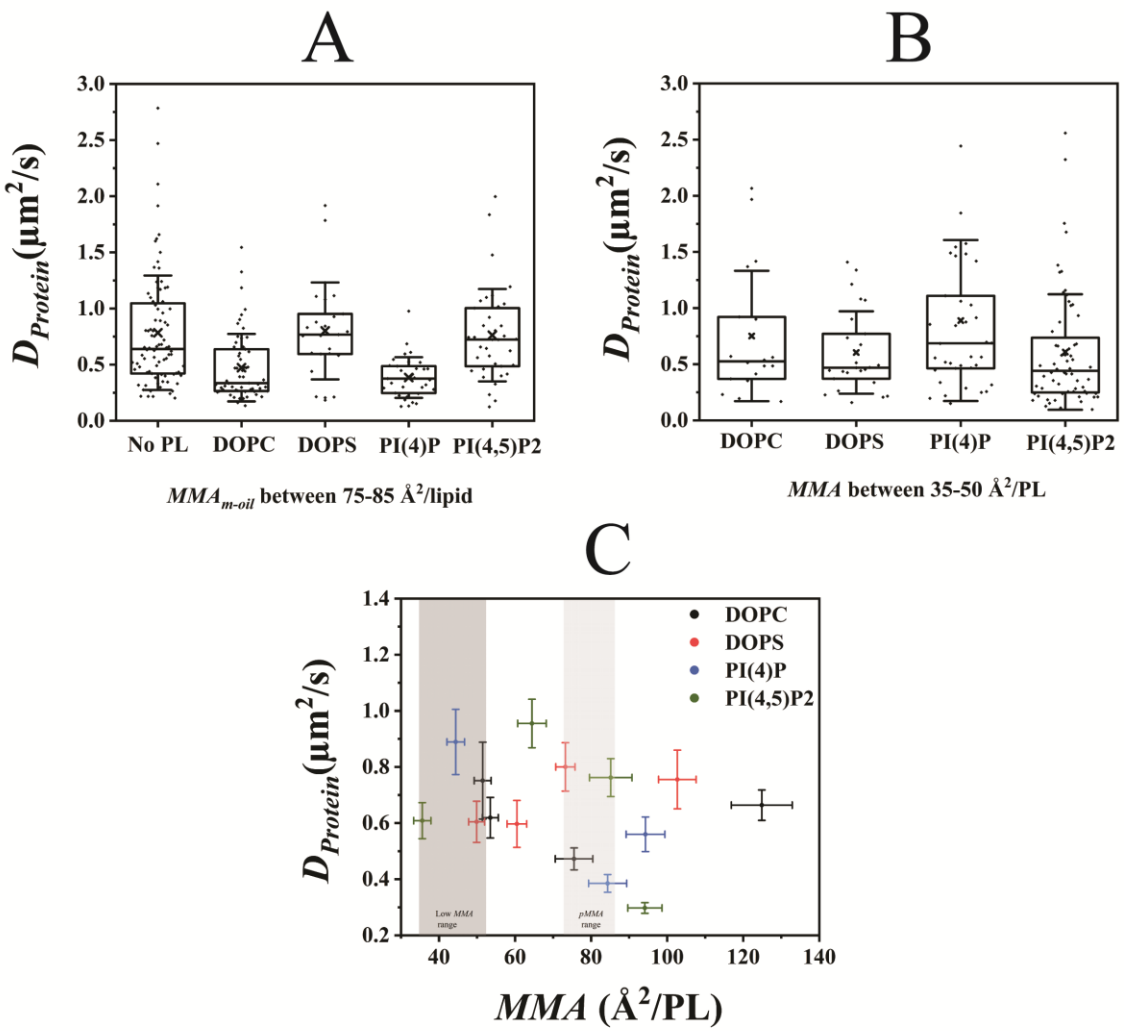

Figure S8: HCC mobility depends weakly on ALD monolayer composition and *MMA*.
AF488-labelled HCC mobility was quantified via lsFCS for the same ALD monolayers as in **Figures 1C**, **D** or **S4** and represented here as protein diffusion coefficient ($D_{Protein}$). **A** and **B** represent the distribution of $D_{Protein}$ values for proteins bound to ALD monolayers at *pMMA* and "low *MMA*" conditions, respectively. The ALD monolayers were composed of DOPC, DOPC+DOPS (9:1), DOPC+PI(4)P (9:1) and DOPC+PI(4,5)P2 (9:1). **A** additionally shows $D_{Protein}$ data for ALDs made only with oil, i.e. bare oil droplets. Each point represents the result of one lsFCS measurement within one ALD. In all box plots, the horizontal line represents the median value, while the 'x' indicates the mean with the first and third quartile as the boundaries. The whiskers indicate SDs. Data points were pooled from at least 3 independent experiments. **C** shows the $D_{Protein}$ values as a function of ALD monolayer *MMA*. *MMA* values were not directly measured but rather estimated from PL/oil ratios and protein-free ALDs, as indicated on **Table S5**. Light grey and dark grey boxes show the *pMMA* range and "low *MMA*" range respectively. Here, each point represents the mean values of each of the two parameters obtained from at least 18-59 experimental points for DOPC ALDs, 25-37 points for DOPS mixed ALDs, 33-38 points for PI(4)P mixed ALDs and 32-64 points for PI(4,5)P2 mixed ALDs (see **Table S5**) with error bars as SEM. ALD monolayers were labelled with 0.001 molar% Rh-PE. See **Tables S2**, **S3** and **S5** for the details on the statistics.

537 *2. Cysteine bridges are needed for effective HCC binding to ALDs*

538

539 It is known that the HCC forms dimers via inter-protein disulphide bonds [18]. Such dimers have been shown to
540 be important for capsid stabilization, virus particle production [5,24] and HCC-membrane interaction [5].
541 In comparison to non-reducing conditions (**Figures 1C** and **1E**), we found that the binding of HCC to ALDs,
542 irrespective of the monolayer PL composition, is significantly hindered in a reducing environment, as
543 evidenced by a ~5- to 10-fold decrease in the measured fluorescence intensity signal of the protein at the
544 surface of ALDs (**Figures 2A** and **B**). Interestingly, lsFCS analysis reported the strongest decrease in protein-
545 protein interactions for DOPC ALDs (cf. **Figures S6A** and **2C**). Finally, the decrease in protein binding to
546 ALDs does not appear to significantly modulate protein dynamics at the monolayer interface (cf. **Figures S8A**
547 and **S9**).

548

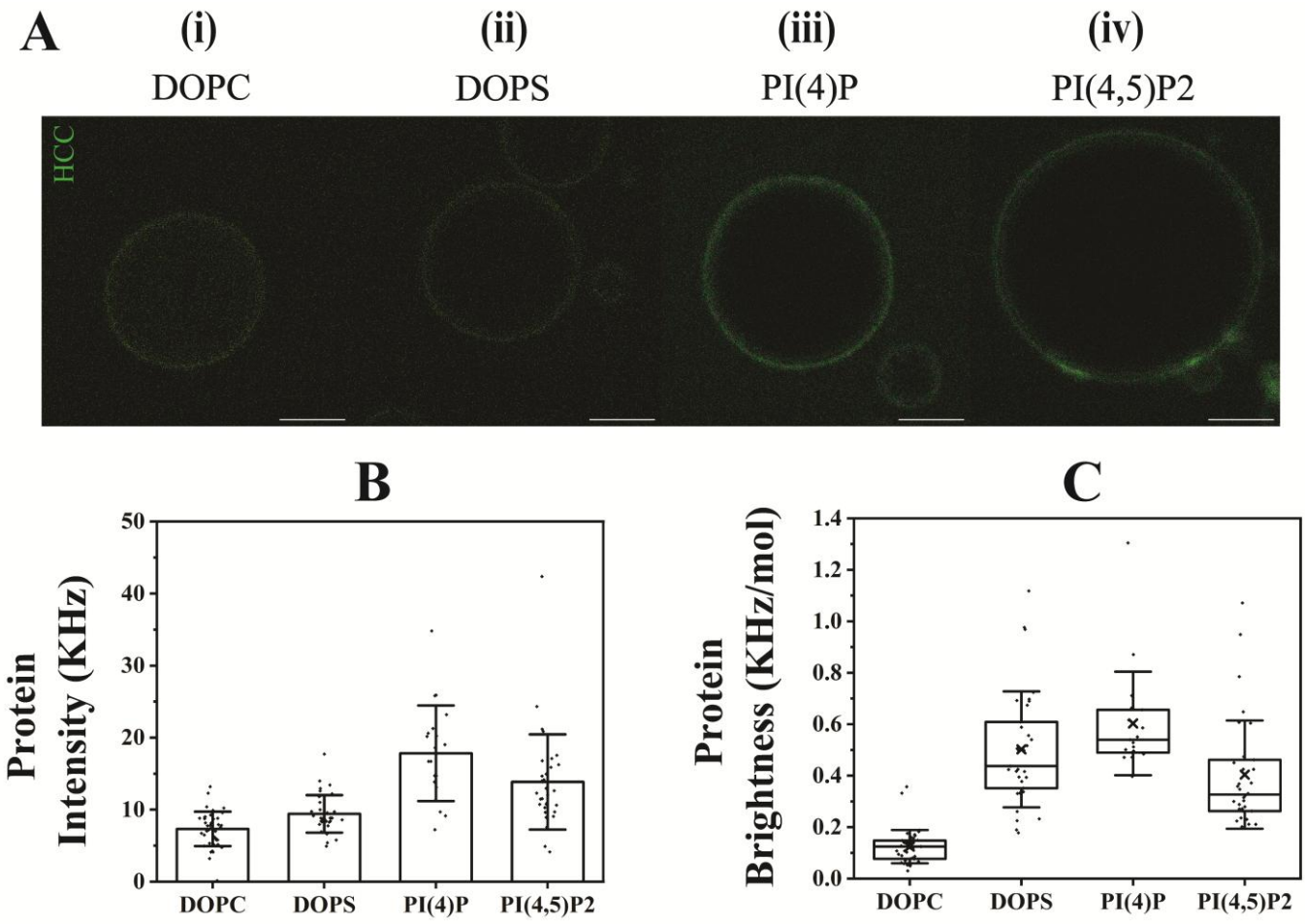

549

550 **Figure 2: Decreased binding of HCC to ALD monolayers at *pMMA* in reducing environment.**
551 Quantification of AF488 labelled HCC binding and multimerization on ALD monolayers at *pMMA* condition was
552 performed in reducing environment via lsFCS analysis and is represented as fluorescent protein intensity and brightness
553 respectively. **A** shows typical fluorescence images of HCC-ALD interaction in reducing environment, **(i)** for ALDs made
554 from DOPC, **(ii)** for ALDs made from DOPC+DOPS (9:1), **(iii)** for ALDs made from DOPC+PI(4)P (9:1) and **(iv)** for
555 ALDs made from DOPC+PI(4,5)P2 (9:1). For enhanced visibility, the intensity range in **(i)** and **(ii)** was reduced by a
556 factor of 9 and that in **(iii)** and **(iv)** by a factor of 4.5 with respect to that of **Figure 1E (i)** (green channel) using Fiji
557 software. The scale bar is 5 µm. **B** shows the fluorescent protein intensity on ALDs derived from images exemplified in

A, as bar graphs. All bars represent mean values with whiskers as the SD. **C** shows the protein brightness values of HCC after binding to the same set of ALDs, in the form of box plots. In all box plots, horizontal line is the median, 'x' marks the mean with first and third quartile as the boundaries and whiskers as SD. All data points were obtained from at least two independent experiments. Reducing environment was obtained through the addition of 5 % β-mercaptoethanol (v/v). Significant differences exist (calculated using one way ANOVA at significance level= 0.05) between protein brightness values for DOPC and the other samples. See **Table S4** for the numerical values.

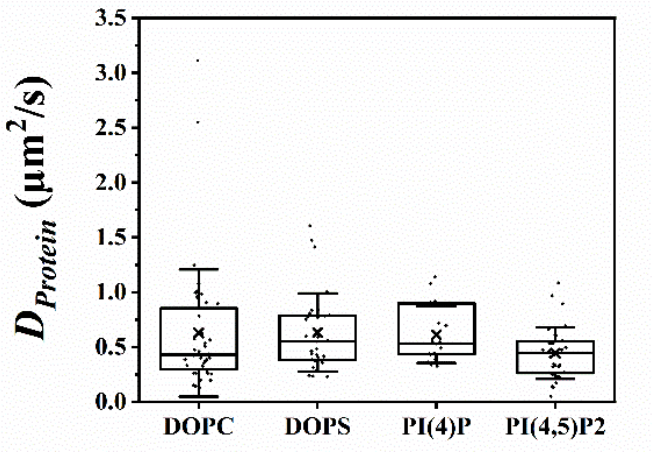

Figure S9: HCC mobility on ALD monolayers at *pMMA* is not strongly affected by reducing environment. Quantification of AF488 labelled HCC mobility via lsFCS in reducing environment on the same ALD monolayers as in **Figures 2A** and **B**, represented as protein diffusion coefficient ($D_{Protein}$). $D_{Protein}$ values for HCC associated to ALD monolayers composed of DOPC, DOPC+DOPS (9:1), DOPC+PI(4)P (9:1) and DOPC+PI(4,5)P2 (9:1) presented as box plots. In all box plots, horizontal line is the median, 'x' marks the mean with first and third quartile as the boundaries and whiskers as SD. All data points were obtained from at least two independent experiments. Reducing environment was obtained through the addition of 5 % β-mercaptoethanol (v/v). See Table **S4** for the numerical values.

3. *Anionic PLs are needed for the binding of HCC to PL bilayers*

In cells, removal of the SP from HCC results in its subsequent transfer from the ER bilayer to LD [25], which are the sites of HCC multimerization - as a fundamental step of capsid assembly [15]. Eventually, the HCC returns from the LD back to the ER bilayer [14,26] and this re-targeting is crucial for efficient formation of virions [31] (see **Introduction**). While it was reported that the D2 domain of HCC binds to bilayers exclusively in the presence of TG in the interleaflet region [33], the role of anionic PLs in this process has not been addressed yet. Therefore, we have investigated the interaction between HCC and GUVs containing different anionic PLs.

The binding of HCC to these bilayers is in general significantly (between one and two orders of magnitude) lower than to ALDs at *pMMA* (**Figures 3A** and **B,** cf. with **Figures 1E** and **C**). Interestingly, a fluorescence signal from the bound protein significantly above the background was observed exclusively in the presence of anionic PLs (**Figure 3A**). Probably due to the low concentration at the membrane, HCC does not significantly oligomerize, for all analysed compositions, as evidenced by molecular brightness values well

591 below those measured for ALD-bound proteins (cf. **Figures 3C** and **S6A**). LsFCS analysis also shows that
592 diffusive dynamics of HCC on the GUV surface, i.e. $D_{Protein}$ values, are ~3 times faster than HCC bound to
593 ALDs at *pMMA*, irrespective of the PL composition (**Figure 3D**). It is worth noting that HCC brightness/
594 multimerization measurements and diffusion coefficient quantification were not possible for GUVs containing
595 exclusively DOPC, as the fluorescence signal from the bound protein was not sufficiently high for lsFCS
596 analysis. Interestingly, as already observed for the case of LDs, both HCC and PL lateral organization on
597 bilayers is heterogeneous in the presence of anionic PLs (**Figure 3A**). Finally, **Figure S10** shows that HCC-
598 HCC interactions are correlated to the local protein concentration, similar (albeit showing lower concentration
599 and multimerization values) to what is observed in ALD systems (**Figure S7A**).

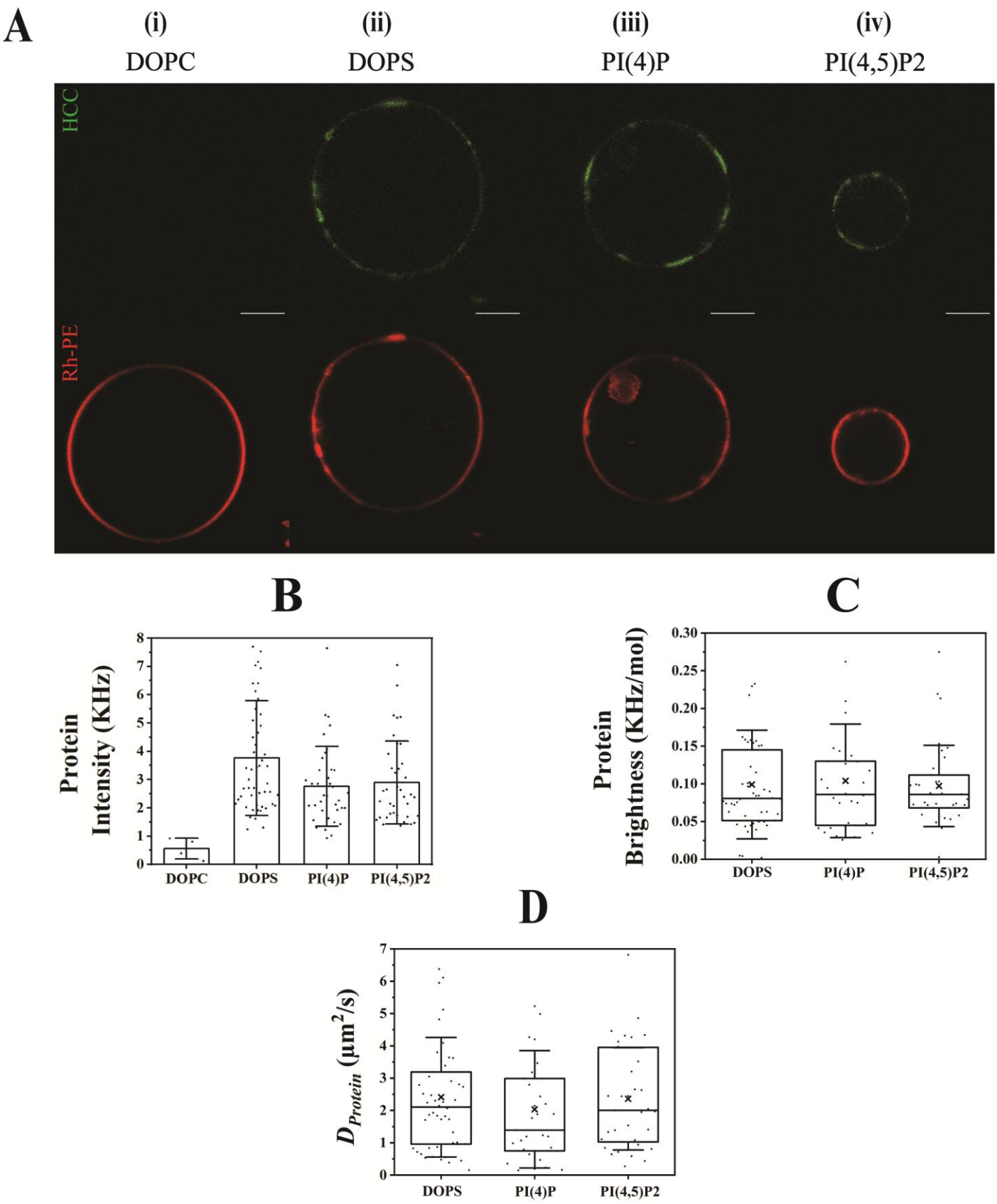

Figure 3: HCC binds to bilayer models only in the presence of anionic PLs.
Quantification of AF488 labelled HCC binding, multimerization and mobility via lsFCS analysis on GUVs composed of different PL species represented as protein intensity, brightness and diffusion coefficient ($D_{Protein}$). **A** shows the fluorescence images of HCC-GUV interaction. As shown, **(i)** for GUVs made from DOPC, **(ii)** for GUVs made from DOPC+DOPS (9:1), **(iii)** for GUVs made from DOPC+PI(4)P (9:1) and **(iv)** for GUVs made from DOPC+PI(4,5)P2 (9:1). For each column, green channel (top) shows the AF488 labelled HCC, and the red channel (bottom) shows Rh-

PE labelled GUV. For enhanced visibility, the displayed intensity range of all red channel images was increased by a factor of 3 and that of the green channel was decreased by 9 times with respect to that of **Figure 1E (i)** using Fiji software. Scale bar is 5 µm. **B** shows the fluorescent protein intensity on GUVs quantified from images exemplified in **A**, shown as bar graph. All bars represent mean values with whiskers as the SD. **C** and **D** show the distribution of protein brightness and $D_{Protein}$ values from HCC binding to the same set of GUVs (except DOPC) in the form of box plots. GUVs of all PL compositions were labelled with 0.005 molar% Rh-PE for visualization purpose. In all box plots (**C** and **D**), horizontal line is the median, 'x' marks the mean with first and third quartile as the boundaries and whiskers as SD. All data points were obtained from at least three independent experiments. See **Table S7i** for the numerical values.

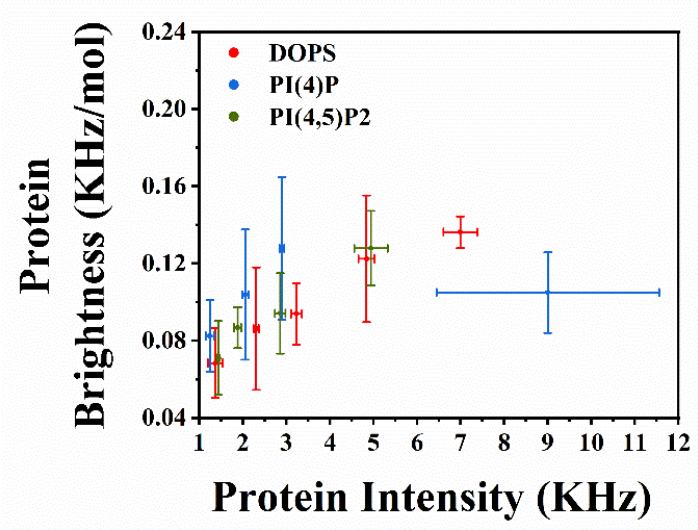

Figure S10: HCC limited oligomerization as a function of its concentration on GUVs.
Intensity and brightness data points from **Figures 3B** and **C** were plotted relative to each other. For easy viewing purpose, the data points were binned such that each point represents the mean value calculated from 5-12 points for DOPS mixed GUVs, 5-10 points for PI(4)P mixed LDs and 5-11 points for PI(4,5)P2 mixed LDs. Error bars are SEM. See **Tables S7ii-iv** for the data points.

4. HCC forms µm-scale clusters in both GUVs and ALDs in the presence of anionic PLs

Studies in cell models have reported the formation of HCC dimers to be followed by multimerization and large-scale assembly to finally form the HCV capsid [7]. Up to this point in our study, lsFCS has been used to quantify HCC oligomerization, but this approach is limited to (ideally diffraction-limited) mobile protein assemblies [41]. On the other hand, larger and less mobile protein clusters (such as those observed in **Figures 1E** and **3A**) can be quantified via ICS [42]. The observed inhomogeneity in the lateral organization of HCC both in ALDs (**Figure 1E**) and GUVs (**Figure 3A**) appears to be spatially correlated with regions in the membrane enriched with the fluorescent PL marker Rh-PE. In order to quantify HCC clustering as a function of PL composition, we used ICS to calculate the degree of clustering (*DOC*) , defined as the ratio between average fluorescence intensity and cluster density [42] (see **Methods**).

According to this analysis (**Figure 4**), and in line with the qualitative visual inspection of **Figures 1E** and **3A**, HCC forms clusters exclusively in samples containing anionic PLs. Specifically, in the case of ALDs, HCC clusters are evident in samples containing 10 mol% DOPS, PI(4)P and PI(4,5)P2, but not in samples

640 constituted of 100 mol% DOPC. Similar results are observed in GUVs, although the *DOC* is in general
641 considerably lower than in ALD with a similar composition. The protein clusters and oligomers observed in
642 our assays appear to be indeed established via interactions which are relevant for virus assembly, as the
643 assembly-incompetent HCC mutant Δ68 [45], under similar surface concentration, exhibits a strong decrease
644 both in protein brightness and *DOC* in PI(4)P mixed ALDs (**Figure S11**).
645

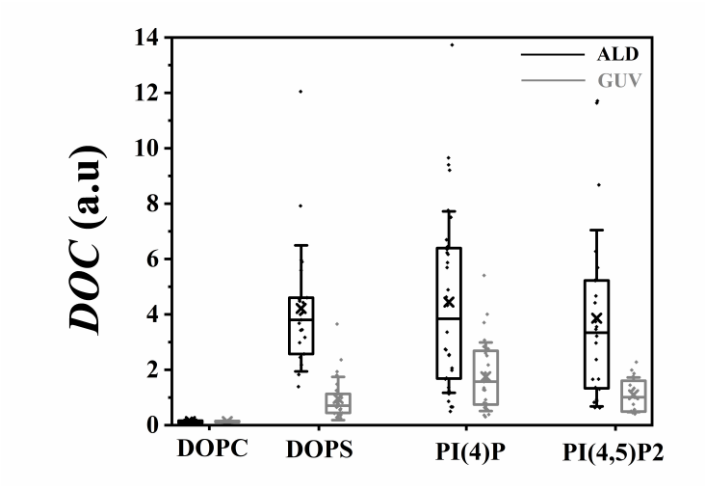

646
647 **Figure 4: Anionic PLs induce HCC large-scale clusters in mono- and bilayer models.**
648 Large-scale AF488 labelled HCC clusters in ALDs (at *pMMA*) and GUVs composed of DOPC, DOPC+DOPS (9:1),
649 DOPC+PI(4)P (9:1) and DOPC+PI(4,5)P2 (9:1) were quantified using ICS and the derived degree of clustering (*DOC*).
650 All values are shown as box plots with the data points obtained from three independent experiments. ALD data points
651 are shown in black boxes, and GUV data points are shown in grey boxes. In all box plots, horizontal line marks the
652 median, 'x' marks the mean with first and third quartile as the boundaries and whiskers as SD. See **Table S8** for the
653 numerical values.
654

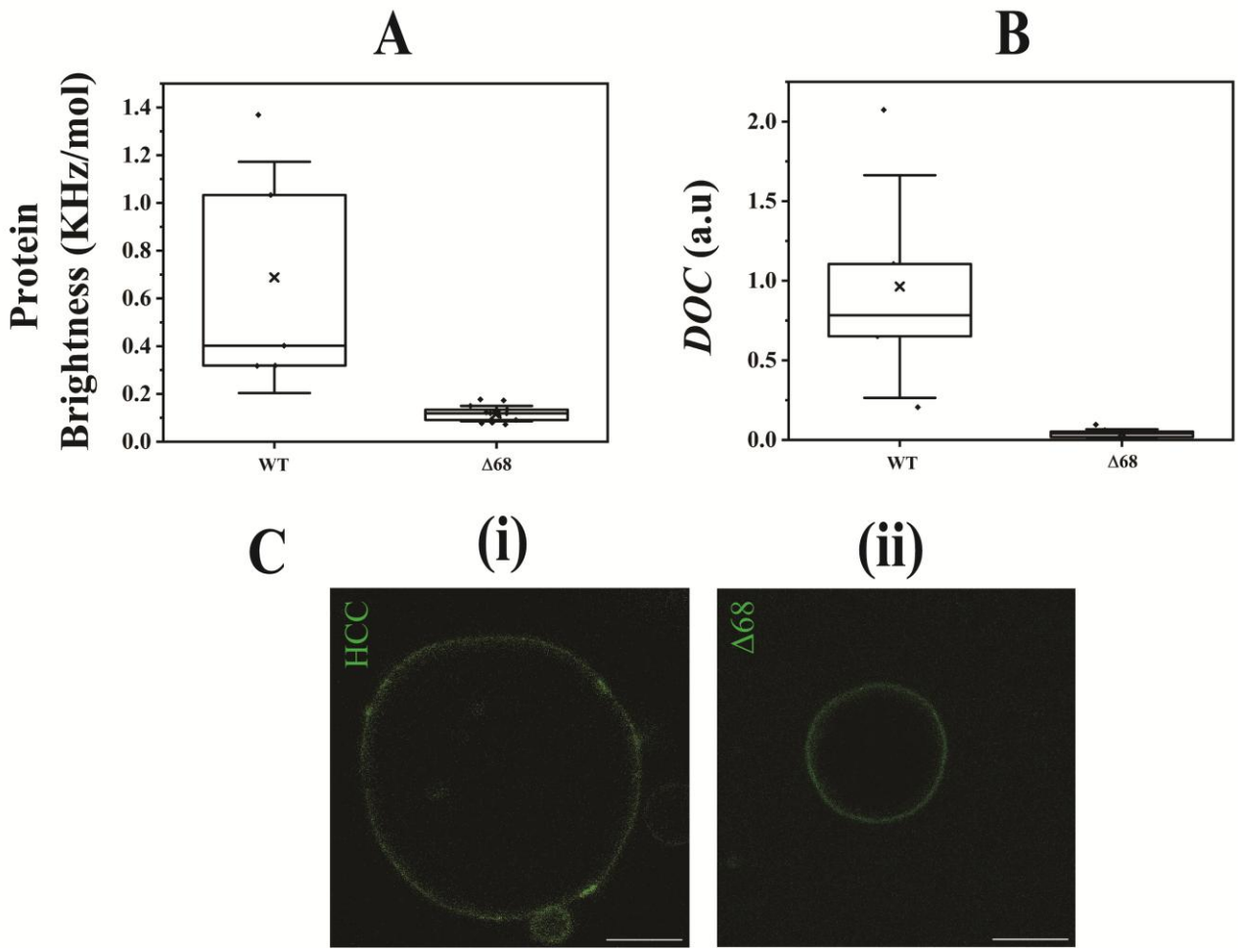

Figure S11: Comparison of clustering and multimerization between HCC and assembly-incompetent HCC mutant Δ68 on ALDs.

Quantification of protein (HCC and Δ68) multimerization and clustering was performed on the same type of ALD (*pMMA* condition) composed of DOPC+PI(4)P (9:1) using lsFCS and ICS, represented as protein brightness (**A**) and degree of clustering (*DOC*) (**B**) respectively. Protein concentration was similar (~10-20 KHz) for all measured samples. All values are shown as box plots. In all box plots, horizontal line marks the median, 'x' marks the mean with first and third quartile as the boundaries and whiskers as SD. Each data point represents a measurement from a single ALD. See **Table S9** for the numerical values. **C** shows the fluorescence images of HCC- (or Δ68-) ALD interaction. For enhanced visibility, the displayed intensity range of all green channels was decreased by 9 times with respect to that of **Figure 1E (i)** using Fiji software. Scale bar is 5 µm.

5. *HCC binding decreases PL dynamics in ALD monolayers*

In order to test the effect of protein binding on PL dynamics, we monitored the diffusion of the fluorescent PL analogue Rh-PE (D_{PL}). The underlying assumption here is that the viscosity and the local membrane environment sensed by the fluorescent PL are a good approximation of those sensed by the rest of the PLs [39]. Irrespective of the PL species, D_{PL} in ALD monolayers at *pMMA* is strongly decreased (~10-fold) following HCC binding (**Figure 5**). Interestingly, a decrease in lateral dynamics was also observed for a structurally different fluorescent PL analogue TF-PC ($D_{PL/TF\text{-}PC}$), albeit not to a much lower extent (i.e., ~3-fold decrease) (**Figure S11**).

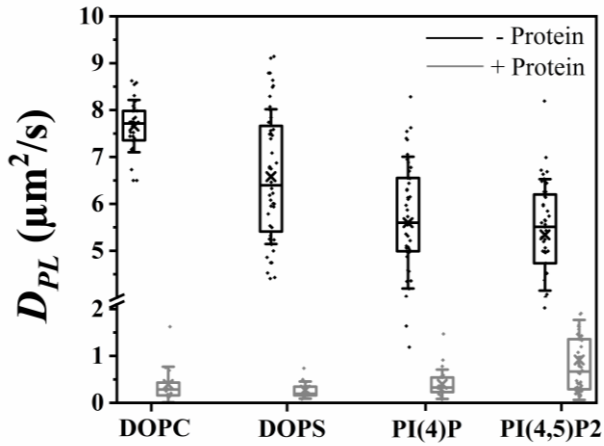

Figure 5: ALD monolayer PL mobility decreases as a consequence of HCC binding.
PL mobility in ALD monolayers composed of DOPC, DOPC+DOPS (9:1), DOPC+PI(4)P (9:1) and DOPC+PI(4,5)P2 (9:1) at *pMMA* (labelled with 0.001 molar% Rh-PE), represented as D_{PL} was analysed by lsFCS. All values are shown in the form of box plots with the data points from two to three independent experiments. The data points for ALDs without HCC are depicted in black boxes and those in the presence of HCC in grey boxes. In all box plots, the horizontal line marks the median, 'x' marks the mean with first and third quartile as the boundaries and whiskers as SD. See **Table S10** for the numerical values.

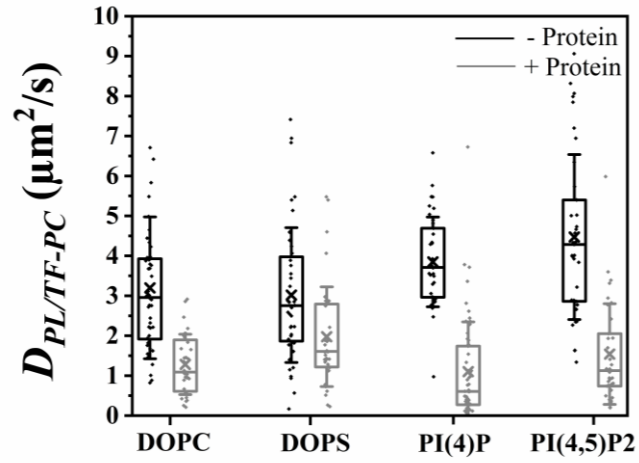

Figure S12: Effect of HCC binding on monolayer PL mobility measured using TF-PC.
PL mobility on ALDs composed of DOPC, DOPC+DOPS (9:1), DOPC+PI(4)P (9:1) and DOPC+PI(4,5)P2 (9:1) at *pMMA* (labelled with 0.005 molar% TF-PC), represented as $D_{PL/TF-PC}$ was analysed by lsFCS. All values are shown as box plots with the data points obtained from three independent experiments. The data points for ALDs without HCC are depicted in black boxes and those in the presence of HCC in grey boxes. In all box plots, the horizontal line marks the median, 'x' marks the mean with first and third quartile as the boundaries and whiskers as SD. See **Table S10** for the numerical values.

Discussion

The binding of the HCC protein to the LD monolayer surface and subsequent return to the ER bilayer membrane is a fundamental step of the HCV capsid assembly [4,14,15,26]. In this complex process, the role of lipid molecules is not known yet, despite the evidence of significant upregulation of certain PL species in the HCV infectious cycle [8,34,66]. In this work, we aimed to investigate the possible function of specific lipids in HCC assembly.

Previous studies regarding HCC-LD interaction did not address this aspect [16,67,68]. A more recent study by Ajjaji and colleagues [33] highlighted the importance of triglycerides in the interaction between HCC and monolayers or bilayers. However, these results were based on the investigation of ALD monolayers composed of only DOPC and DOPE, thereby not addressing the possible effect of other (e.g. anionic) PLs, which are synthetized more abundantly during HCV infection [36]. Our experiments suggest that, irrespective of PL composition, the LD monolayer constitutes in general a passive barrier to HCC-LD interaction, as HCC shows the highest binding to oil droplets devoid of PLs. In analogy, HCC binding decreases dramatically, as more and more DOPC molecules are included in the monolayer (**Figure S4**). A previous study showed a similar effect, albeit for a specific domain (i.e., D2) of this protein [33]. The oil-protein interaction seems therefore to dominate over possible lipid-protein interactions and, in fact, anionic PLs do not appear to strongly modulate HCC-LD interaction, at least under physiological monolayer packing density (**Figure 1**). In these conditions, monolayer packing defects might be present [69] and HCC might use such defects to interact with the oil phase (possibly via its amphipathic helix), rather than with (anionic) PLs [15,33]. Similar behaviour is observed for several LD-binding proteins [69,70]. On the other hand, HCC interactions with specific anionic PLs become evident at higher PL packing (**Figure S4**), as increasing monolayer PL density enhances HCC-LD binding in the presence of e.g. PI(4,5)P2, opposite to what observed for the zwitterionic DOPC.

The dominant role of HCC-oil phase interactions might also explain why individual PL species do not show overall dramatic effects on other investigated biophysical properties of HCC on the LD (i.e. multimerization and mobility, **Figures S6** and **S8**). Nevertheless, we observed that at least one negatively charged PL (i.e., PI(4)P) appears to enhance HCC concentration-dependant multimerization (**Figures S7A** and **B**). Of interest, in our ALD models, HCC form multimers of up to ca. 50-60 subunits (at a concentration of ca. 2500 mol/µm² and in the presence of PI(4)P), i.e. with a size similar to what is expected for the HCV capsid [45,71–73]. The apparent role of PI(4)P in facilitating capsid formation might relate to the observation that HCV infection is marked by high intracellular concentrations of this particular PL [36].

Further evidence of the role of anionic lipids in modulating HCC-HCC interactions comes from the observation of large-scale protein clusters, spatially correlated to anionic PL assemblies (**Figure 4**). Since negatively-charged PL form such platforms also in the absence of the protein (see **Figure S3A** and previous studies [74–76]), we hypothesize that HCC-HCC interactions might be stabilized as a consequence of binding to

these PL platforms, through an increase in local protein concentration. Also, it is worth noting that, although PI(4)P is not the only anionic PL forming clusters in ALDs, this PL appears to have a stronger effect on the formation of HCC oligomers (**Figure S7B**), thus suggesting the additional possibility of specific HCC-PI(4)P interactions that might potentially alter HCC-HCC affinity.

Since these large-scale protein assemblies are significantly larger than the microscope resolution (i.e., ca. 250 nm [77]) and the *DOC* varies over a range of ~40-fold, it is safe to assume that such clusters are not single capsids but rather either larges assemblies of multiple capsids or more disordered protein assemblies. While imaging approaches with higher resolution are needed for a more in-depth characterization of the observed protein assemblies [78], it must be noted that the protein-protein interactions quantified in this work are at least analogous to the interactions observed *in vivo* during HCV assembly, as demonstrated by the decreased multimerization (both in terms of large-scale clusters characterized via ICS or microscopic multimers characterized via lsFCS) in the case of the assembly-incompetent mutant HCC mutant Δ68 [45,78] (**Figure S11**).

The conclusion that anionic PLs in the LDs increase HCC-HCC interactions is further strengthened by experiments in reducing conditions (**Figure 2**). While inter-HCC cysteine bridges have been proposed to stabilize the capsid and thereby control the viral assembly process [5,24], our data further suggest a role in protein binding to the monolayer. Specifically, while protein multimerization is, as expected, strongly decreased in reducing conditions for the case of DOPC monolayers, HCC multimers are instead apparently stabilized by the presence of negatively charged PLs. Of note, this behaviour – similarly to the other effects of negatively-charged PLs on HCC-HCC or HCC-lipid interactions observed in this work – does not seem to correlate with the amount of negative charges in the anionic PLs, once more hinting at the possibility of specific (rather than unspecific electrostatic) interactions between these PLs and HCC.

So far, the observations of HCC binding to tightly packed monolayers and the high affinity of the protein for the oil core of LD devoid of PLs are compatible with the hypothesis that the protein interacts with the oil phase and, concurrently, to anionic PLs via electrostatic interactions. Also, the presence of direct, albeit weak, interactions between HCC and negatively charged PLs is confirmed by our experiments on model bilayers (**Figure 3)**. While triglycerides were shown to promote the binding of HCC to bilayers [33] (e.g. to the ER), we demonstrate here that the presence of small concentrations of anionic PLs is also sufficient to obtain a protein binding significantly higher than that observed in the presence of only zwitterionic PLs. Of note, HCC binding to bilayers is nevertheless much lower than the one observed in the case of monolayers and, as expected, is associated to much weaker protein-protein interactions (due to lower local concentration on the membrane, see **Figure S10**). In this context, the much slower diffusive dynamics of HCC on monolayers compared to bilayers (cf. **Figure 3D** and **S8C**) suggest that the protein binds only superficially to bilayers (i.e. to PL headgroups [39]). On the other hand, in monolayers, the protein might at least partially insert into the highly viscous oil-phase [33], thus slowing down its lateral diffusion.

The last part of our work focuses on the effect of protein binding on the properties of the lipids in the LD monolayer. Since we hypothesize that direct interactions might exist between anionic PLs and oligomers (or

large multimers) of HCC, it is reasonable to expect that protein binding might affect the lateral diffusion of PLs in the membrane [79,80]. Furthermore, it was also reported that PL dynamics is affected by the insertion of proteins into a monolayer or a membrane leaflet [80,81]. Accordingly, our results indicate a strong decrease in diffusive dynamics of a fluorescent PL probe (Rh-PE) after binding of HCC to the monolayer (**Figure 5**). Interestingly, the diffusion of a structurally different fluorescent PL (TF-PC) also decreases in the presence of a protein, but to a much smaller extent. Assuming that Rh-PE carries a negative charge at pH 7.4, while TF-PC remains neutral, the latter PL probe would report a general decrease in diffusive dynamics for all PLs in the monolayer (due e.g. to the insertion of the protein and the consequent increase in PL packing). On the other hand, the dramatic decrease of diffusive dynamics of Rh-PE might instead indicate that this anionic fluorescent PL (similarly to the other anionic PLs in the monolayer) binds to the bulky protein multimers and, as a consequence, diffuses at a much slower rate.

In conclusion, this work shows that anionic PLs affect HCC multimerization on both monolayers (as models of LDs) and bilayers (as models of the ER), probably by modulating the local concentration of the protein. In this scenario, HCC can be hypothesized to interact with the neutral lipid core of LD and concurrently, although possibly weakly, with the polar heads of negatively charged PLs. Such significant involvement of anionic PLs could be one of the reasons why these are more abundant during HCV infection [8,34,36]. Furthermore, we show that, through insertion in the monolayer or by recruiting specific PLs, HCC has the potential to alter the biophysical properties of LD monolayers. While the simplified model system used in this work was necessary to pinpoint specific lipid-protein interactions, future studies should investigate the role of more complex, physiologically relevant lipid compositions and, most importantly, the role of other host or viral proteins.

References

1. World Health Organization, HCV, Assessed on June 12, 2024. https://www.who.int/news-room/fact-sheets/detail/hepatitis-c#:~:text=Globally%2C%20an%20estimated%2058%20million,with%20chronic%20hepatitis%20C%20infection.

2. National Health Service, 2022, Hepatitis. Assessed on June 12, 2024. https://www.nhs.uk/conditions/hepatitis/.

3. Adugna, A. Therapeutic strategies and promising vaccine for hepatitis C virus infection. *Immun Inflamm Dis* **11**, (2023).

4. Gawlik, K. & Gallay, P. A. HCV core protein and virus assembly: what we know without structures. *Immunol Res* **60**, 1–10 (2014).

5. Kushima, Y., Wakita, T. & Hijikata, M. A Disulfide-Bonded Dimer of the Core Protein of Hepatitis C Virus Is Important for Virus-Like Particle Production. *J Virol* **84**, 9118–9127 (2010).

6. Matsumoto, M., Hwang, S. B., Jeng, K.-S., Zhu, N. & Lai, M. M. C. *Homotypic Interaction and Multimerization of Hepatitis C Virus Core Protein*. *VIROLOGY* vol. 218 (1996).

813 7. Ai, L.-S., Lee, Y.-W. & Chen, S. S.-L. Characterization of Hepatitis C Virus Core Protein Multimerization
814 and Membrane Envelopment: Revelation of a Cascade of Core-Membrane Interactions. *J Virol* **83**, 9923–
815 9939 (2009).

816 8. Syed, G. H., Amako, Y. & Siddiqui, A. Hepatitis C virus hijacks host lipid metabolism. *Trends in*
817 *Endocrinology & Metabolism* **21**, 33–40 (2010).

818 9. Thaker, S. K., Ch'ng, J. & Christofk, H. R. Viral hijacking of cellular metabolism. *BMC Biol* **17**, 59 (2019).

819 10. Mani, H., Yen, J.-H., Hsu, H.-J., Chang, C.-C. & Liou, J.-W. Hepatitis C virus core protein: Not just a
820 nucleocapsid building block, but an immunity and inflammation modulator. *Tzu Chi Med J* **34**, 139
821 (2022).

822 11. Ray, R. B. & Ray, R. Hepatitis C virus core protein: intriguing properties and functional relevance. *FEMS*
823 *Microbiol Lett* **202**, 149–156 (2001).

824 12. Jackel-Cram, C., Babiuk, L. A. & Liu, Q. Up-regulation of fatty acid synthase promoter by hepatitis C virus
825 core protein: Genotype-3a core has a stronger effect than genotype-1b core. *J Hepatol* **46**, 999–1008
826 (2007).

827 13. Paracha, U. Z. *et al.* Oxidative stress and hepatitis C virus. *Virol J* **10**, 251 (2013).

828 14. Shavinskaya, A., Boulant, S., Penin, F., McLauchlan, J. & Bartenschlager, R. The Lipid Droplet Binding
829 Domain of Hepatitis C Virus Core Protein Is a Major Determinant for Efficient Virus Assembly. *Journal of*
830 *Biological Chemistry* **282**, 37158–37169 (2007).

831 15. Vieyres, G. & Pietschmann, T. HCV Pit Stop at the Lipid Droplet: Refuel Lipids and Put on a Lipoprotein
832 Coat before Exit. *Cells* **8**, 233 (2019).

833 16. Boulant, S. *et al.* Structural determinants that target the hepatitis C virus core protein to lipid droplets.
834 *Journal of Biological Chemistry* **281**, 22236–22247 (2006).

835 17. Izumida, K. & Morita, E. The roles of HCV core protein and its binding host factor in virus assembly and
836 release. *Frontiers in Virology* **4**, (2024).

837 18. Boulant, S., Vanbelle, C., Ebel, C., Penin, F. & Lavergne, J.-P. Hepatitis C Virus Core Protein Is a Dimeric
838 Alpha-Helical Protein Exhibiting Membrane Protein Features. *J Virol* **79**, 11353–11365 (2005).

839 19. Sharma, K. K. *et al.* Analysis of the RNA chaperoning activity of the hepatitis C virus core protein on the
840 conserved 3'X region of the viral genome. *Nucleic Acids Res* **40**, 2540–2553 (2012).

841 20. Ivanyi-Nagy, R. *et al.* Analysis of hepatitis C virus RNA dimerization and core-RNA interactions. *Nucleic*
842 *Acids Res* **34**, 2618–2633 (2006).

843 21. Cristofari, G. The hepatitis C virus Core protein is a potent nucleic acid chaperone that directs
844 dimerization of the viral (+) strand RNA in vitro. *Nucleic Acids Res* **32**, 2623–2631 (2004).

845 22. Kunkel, M., Lorinczi, M., Rijnbrand, R., Lemon, S. M. & Watowich, S. J. Self-Assembly of Nucleocapsid-
846 Like Particles from Recombinant Hepatitis C Virus Core Protein. *J Virol* **75**, 2119–2129 (2001).

847 23. Pérez-Berná, A. J., Veiga, A. S., Castanho, M. A. R. B. & Villalaín, J. Hepatitis C virus core protein binding
848 to lipid membranes: The role of domains 1 and 2. *J Viral Hepat* **15**, 346–356 (2008).

849 24. Murray, C. L., Jones, C. T., Tassello, J. & Rice, C. M. Alanine Scanning of the Hepatitis C Virus Core Protein
850 Reveals Numerous Residues Essential for Production of Infectious Virus. *J Virol* **81**, 10220–10231 (2007).

851 25. Herker, E. *et al.* Efficient hepatitis C virus particle formation requires diacylglycerol acyltransferase-1.
852 *Nat Med* **16**, 1295–1298 (2010).

853 26. Boson, B., Granio, O., Bartenschlager, R. & Cosset, F.-L. A Concerted Action of Hepatitis C Virus P7 and
854 Nonstructural Protein 2 Regulates Core Localization at the Endoplasmic Reticulum and Virus Assembly.
855 *PLoS Pathog* **7**, e1002144 (2011).

856 27. Menzel, N. *et al.* MAP-Kinase Regulated Cytosolic Phospholipase A2 Activity Is Essential for Production
857 of Infectious Hepatitis C Virus Particles. *PLoS Pathog* **8**, e1002829 (2012).

858 28. Gentzsch, J. *et al.* Hepatitis C Virus p7 is Critical for Capsid Assembly and Envelopment. *PLoS Pathog* **9**,
859 e1003355 (2013).

860 29. Fukuhara, T. *et al.* Amphipathic α-Helices in Apolipoproteins Are Crucial to the Formation of Infectious
861 Hepatitis C Virus Particles. *PLoS Pathog* **10**, e1004534 (2014).

862 30. Counihan, N. A., Rawlinson, S. M. & Lindenbach, B. D. Trafficking of Hepatitis C Virus Core Protein during
863 Virus Particle Assembly. *PLoS Pathog* **7**, e1002302 (2011).

864 31. Lindenbach, B. D. & Rice, C. M. The ins and outs of hepatitis C virus entry and assembly. *Nat Rev*
865 *Microbiol* **11**, 688–700 (2013).

866 32. Coller, K. E. *et al.* Molecular Determinants and Dynamics of Hepatitis C Virus Secretion. *PLoS Pathog* **8**,
867 e1002466 (2012).

868 33. Ajjaji, D. *et al.* Hepatitis C virus core protein uses triacylglycerols to fold onto the endoplasmic reticulum
869 membrane. *Traffic* **23**, 63–80 (2022).

870 34. Bishé, B., Syed, G. & Siddiqui, A. Phosphoinositides in the hepatitis C virus life cycle. *Viruses* vol. 4 2340–
871 2358 Preprint at https://doi.org/10.3390/v4102340 (2012).

872 35. Berger, K. L., Kelly, S. M., Jordan, T. X., Tartell, M. A. & Randall, G. Hepatitis C Virus Stimulates the
873 Phosphatidylinositol 4-Kinase III Alpha-Dependent Phosphatidylinositol 4-Phosphate Production That Is
874 Essential for Its Replication. *J Virol* **85**, 8870–8883 (2011).

875 36. Islam, K. U. *et al.* Global Lipidome Profiling Revealed Multifaceted Role of Lipid Species in Hepatitis C
876 Virus Replication, Assembly, and Host Antiviral Response. *Viruses* **15**, (2023).

877 37. Hsu, N. Y. *et al.* Viral reorganization of the secretory pathway generates distinct organelles for RNA
878 replication. *Cell* **141**, 799–811 (2010).

879 38. Prince, A. *et al.* Lipid Specificity of the Fusion of Bacterial Extracellular Vesicles with the Host
880 Membrane. *J Phys Chem B* **128**, 8116–8130 (2024).

881 39. Mandal, T. *et al.* A comparison of lipid diffusive dynamics in monolayers and bilayers in the context of
882 interleaflet coupling. *Biochimica et Biophysica Acta (BBA) - Biomembranes* **1867**, 184388 (2025).

883 40. Ries, J., Chiantia, S. & Schwille, P. Accurate Determination of Membrane Dynamics with Line-Scan FCS.
884 *Biophys J* **96**, 1999 (2009).

885 41. Petrich, A., Dunsing, V., Bobone, S. & Chiantia, S. Influenza A M2 recruits M1 to the plasma membrane: A
886 fluorescence fluctuation microscopy study. *Biophys J* **120**, 5478–5490 (2021).

887 42. Kolin, D. L. & Wiseman, P. W. Advances in Image Correlation Spectroscopy: Measuring Number
888 Densities, Aggregation States, and Dynamics of Fluorescently labeled Macromolecules in Cells. *Cell*
889 *Biochem Biophys* **49**, 141–164 (2007).

890 43. Petrich, A. & Chiantia, S. Influenza A Virus Infection Alters Lipid Packing and Surface Electrostatic
891 Potential of the Host Plasma Membrane. *Viruses* **15**, 1830 (2023).

892 44. Petazzi, R. A., Koikkarah, A. A., Tischler, N. D. & Chiantia, S. Detection of Envelope Glycoprotein
893 Assembly from Old World Hantaviruses in the Golgi Apparatus of Living Cells. *J Virol* **95**, (2021).

45. Klein, K. C., Polyak, S. J. & Lingappa, J. R. Unique Features of Hepatitis C Virus Capsid Formation Revealed by De Novo Cell-Free Assembly. *J Virol* **78**, 9257–9269 (2004).

46. Shirey, C. M., Scott, J. L. & Stahelin, R. V. Notes and tips for improving quality of lipid-protein overlay assays. *Anal Biochem* **516**, 9–12 (2017).

47. Davarinejad, H. *Quantifications of Western Blots with ImageJ*. https://www.yorku.ca/yisheng/Internal/Protocols/ImageJ.pdf.

48. Gandhi, S. A. *et al.* Methods for making and observing model lipid droplets. *Cell Reports Methods* 100774 (2024) doi:10.1016/j.crmeth.2024.100774.

49. Chorlay, A. & Thiam, A. R. Neutral lipids regulate amphipathic helix affinity for model lipid droplets. *Journal of Cell Biology* **219**, (2020).

50. Kim, S. & Swanson, J. M. J. The Surface and Hydration Properties of Lipid Droplets. *Biophys J* **119**, 1958–1969 (2020).

51. Angelova, M. I. & Dimitrov, D. S. *Liposome Electro Formation*. *Faraday Discuss. Chem. SOC* vol. 81 (1986).

52. Stein, H., Spindler, S., Bonakdar, N., Wang, C. & Sandoghdar, V. Production of isolated giant unilamellar vesicles under high salt concentrations. *Front Physiol* **8**, (2017).

53. Petrich, A., Dunsing, V., Bobone, S. & Chiantia, S. Influenza A M2 recruits M1 to the plasma membrane: A fluorescence fluctuation microscopy study. *Biophys J* **120**, 5478–5490 (2021).

54. Petrášek, Z. & Schwille, P. Precise measurement of diffusion coefficients using scanning fluorescence correlation spectroscopy. *Biophys J* **94**, 1437–1448 (2008).

55. Daniels, C. R. *et al.* Fluorescence correlation spectroscopy study of protein transport and dynamic interactions with clustered-charge peptide adsorbents. *Journal of Molecular Recognition* **25**, 435–442 (2012).

56. Cruickshank, C. *The Stokes-Einstein Law Fo r Diffusion in Solution*. *Zeit. fur Elektrochem* vol. 17 https://royalsocietypublishing.org/ (1905).

57. Chenyakin, Y. *et al.* Diffusion coefficients of organic molecules in sucrose–water solutions and comparison with Stokes–Einstein predictions. *Atmos Chem Phys* **17**, 2423–2435 (2017).

58. Perevoshchikova, I. V., Zorov, D. B. & Antonenko, Y. N. Peak intensity analysis as a method for estimation of fluorescent probe binding to artificial and natural nanoparticles: Tetramethylrhodamine uptake by isolated mitochondria. *Biochimica et Biophysica Acta (BBA) - Biomembranes* **1778**, 2182–2190 (2008).

59. Turgeman, L. & Fixler, D. Time-averaged fluorescence intensity analysis in fluorescence fluctuation polarization sensitive experiments. *Biomed Opt Express* **4**, 868 (2013).

60. Dunsing, V. *et al.* Optimal fluorescent protein tags for quantifying protein oligomerization in living cells. *Sci Rep* **8**, 10634 (2018).

61. Moreno-Pescador, G. *et al.* Thermoplasmonic Vesicle Fusion Reveals Membrane Phase Segregation of Influenza Spike Proteins. *Nano Lett* **23**, 3377–3384 (2023).

62. Ries, J. & Schwille, P. Fluorescence correlation spectroscopy. *BioEssays* **34**, 361–368 (2012).

63. Chwastek, G. & Schwille, P. A monolayer assay tailored to investigate lipid-protein systems. *ChemPhysChem* **14**, 1877–1881 (2013).

933 64. Asfia, S., Seemann, R. & Fleury, J.-B. Phospholipids diffusion on the surface of model lipid droplets.
934 *Biochimica et Biophysica Acta (BBA) - Biomembranes* **1865**, 184074 (2023).

935 65. Merten, J. A., Schultz, K. M. & Klug, C. S. Concentration-dependent oligomerization and oligomeric
936 arrangement of LptA. *Protein Science* **21**, 211–218 (2012).

937 66. Borawski, J. *et al.* Class III Phosphatidylinositol 4-Kinase Alpha and Beta Are Novel Host Factor
938 Regulators of Hepatitis C Virus Replication. *J Virol* **83**, 10058–10074 (2009).

939 67. Lyn, R. K., Kennedy, D. C., Stolow, A., Ridsdale, A. & Pezacki, J. P. Dynamics of lipid droplets induced by
940 the hepatitis C virus core protein. *Biochem Biophys Res Commun* **399**, 518–524 (2010).

941 68. Awadh, A. A. The Role of Cytosolic Lipid Droplets in Hepatitis C Virus Replication, Assembly, and
942 Release. *Biomed Res Int* **2023**, (2023).

943 69. Vanni, S. Intracellular Lipid Droplets: From Structure to Function. *Lipid Insights* **10**, 117863531774551
944 (2017).

945 70. Vanni, S., Hirose, H., Barelli, H., Antonny, B. & Gautier, R. A sub-nanometre view of how membrane
946 curvature and composition modulate lipid packing and protein recruitment. *Nat Commun* **5**, 4916
947 (2014).

948 71. Kunkel, M. & Watowich, S. J. Biophysical characterization of hepatitis C virus core protein: Implications
949 for interactions within the virus and host. *FEBS Lett* **557**, 174–180 (2004).

950 72. Katen, S. & Zlotnick, A. Chapter 14 The Thermodynamics of Virus Capsid Assembly. in 395–417 (2009).
951 doi:10.1016/S0076-6879(08)04214-6.

952 73. HAGAN, M. F. Modeling Viral Capsid Assembly. in 1–68 (2014). doi:10.1002/9781118755815.ch01.

953 74. Husby, M. L. *et al.* Phosphatidylserine clustering by the Ebola virus matrix protein is a critical step in viral
954 budding. *EMBO Rep* **23**, (2022).

955 75. Sarmento, M. J., Coutinho, A., Fedorov, A., Prieto, M. & Fernandes, F. Ca2+ induces PI(4,5)P2 clusters on
956 lipid bilayers at physiological PI(4,5)P2 and Ca2+ concentrations. *Biochimica et Biophysica Acta (BBA) -*
957 *Biomembranes* **1838**, 822–830 (2014).

958 76. Wen, Y., Vogt, V. M. & Feigenson, G. W. PI(4,5)P_2 Clustering and Its Impact on Biological Functions. *Annu*
959 *Rev Biochem* **90**, 681–707 (2021).

960 77. Bacia, K., Kim, S. A. & Schwille, P. Fluorescence cross-correlation spectroscopy in living cells. *Nat*
961 *Methods* **3**, 83–89 (2006).

962 78. Klein, K. C., Dellos, S. R. & Lingappa, J. R. Identification of Residues in the Hepatitis C Virus Core Protein
963 That Are Critical for Capsid Assembly in a Cell-Free System. *J Virol* **79**, 6814–6826 (2005).

964 79. Duncan, A. L. *et al.* Protein crowding and lipid complexity influence the nanoscale dynamic organization
965 of ion channels in cell membranes. *Sci Rep* **7**, (2017).

966 80. Iyer, A., Petersen, N. O., Claessens, M. M. A. E. & Subramaniam, V. Amyloids of alpha-synuclein affect
967 the structure and dynamics of supported lipid bilayers. *Biophys J* **106**, 2585–2594 (2014).

968 81. Auerswald, J. *et al.* Measuring protein insertion areas in lipid monolayers by fluorescence correlation
969 spectroscopy. *Biophys J* **120**, 1333–1342 (2021).

970
971
972
973